Exploring and manipulating cardiovascular material properties at an embryonic level

by

Hummaira Banu Siddiqui

A Dissertation Submitted to the
Graduate School of Sciences and Engineering
in Partial Fulfilment of the Requirements for
the Degree of

Master of Science

in

Biomedical Engineering

KOÇ
ÜNİVERSİTESİ

August 15, 2022

Exploring and manipulating cardiovascular material properties at an embryonic level

Koç University

Graduate School of Sciences and Engineering

This is to certify that I have examined this copy of a master's thesis by

Hummaira Banu Siddiqui

and have found that it is complete and satisfactory in all respects,
and that any and all revisions required by the final
examining committee have been made.

Committee Members:

_____

Prof./ Assoc. Prof / Assist. Prof. Kerem Pekkan (Advisor)

_____

Prof./ Assoc. Prof / Assist. Prof. Mehmet Sayar (Jury Member)

_____

Prof./ Assoc. Prof / Assist. Prof. Pinar Yilgor Huri (Jury Member)

Date: 16.09.2022

To my Professor Kerem Pekkan who showed me the real purpose of an education and believed in me

ABSTRACT

Exploring and manipulating cardiovascular material properties at an embryonic level

Hummaira Banu Siddiqui

Master of Science in Biomedical Engineering

August 15, 2022

The embryonic system is the precursor for the mature cardiovascular system. This thesis focuses on studying the material properties at the embryonic level and then devising a method to manipulate these properties such that physiological changes caused by congenital heart diseases (CHD's) can be eliminated prior to birth. The main focus is compiling the cardiovascular embryonic material properties and their relation to specific mechanosensitive and mechanoresponsive genes through an extensive review of all available literature. The compilation of embryonic mechanical properties will also contribute to our understanding of the mature cardiovascular system and possibly lead to new microstructural and genetic interventions to correct abnormal development. Using this data, a comparison and manipulation of genes was enabled which in turn controlled the physiology of the aortic arch region in chick embryos. The targeted material properties were elasticity and stiffness which were controlled by TGFb3 and MMP2 respectively. Our results showed that localized genetic modification of the aortic arch region governs the physiology of the embryo and hence will reduce the risk of CHD (congenital heart disease) development at later stages of growth and prevent the need for surgical interventions after birth. This approach can be combined with mechanical intervention models including conotruncal banding and left atrial ligation models of chick embryo.

Word Count: 210 words

ÖZETÇE

Embriyonik düzeyde kardiyovasküler malzeme özelliklerini keşfetmek ve manipüle etmek

Hummaira Banu Siddiqui

Biomedical Muhendislik, Yüksek Lisans

Ağustos 15, 2022

Embriyonik sistem, olgun kardiyovasküler sistemin öncüsüdür. Bu tez, materyal özelliklerini embriyonik düzeyde incelemeye ve daha sonra bu özellikleri, doğuştan kalp hastalıklarının (KKH'ler) neden olduğu fizyolojik değişikliklerin doğumdan önce ortadan kaldırılabileceği şekilde manipüle etmek için bir yöntem geliştirmeye odaklanmaktadır. Ana odak, kardiyovasküler embriyonik materyal özelliklerini ve bunların belirli mekanik duyarlı ve mekanik yanıt veren genlerle olan ilişkisini, mevcut tüm literatürün kapsamlı bir incelemesi yoluyla derlemektir. Embriyonik mekanik özelliklerin derlenmesi ayrıca olgun kardiyovasküler sistemi anlamamıza katkıda bulunacak ve muhtemelen anormal gelişimi düzeltmek için yeni mikroyapısal ve genetik müdahalelere yol açacaktır. Bu verileri kullanarak, civciv embriyolarında aortik ark bölgesinin fizyolojisini kontrol eden genlerin bir karşılaştırması ve manipülasyonu sağlandı. Hedeflenen malzeme özellikleri, sırasıyla TGFb3 ve MMP2 tarafından kontrol edilen elastikiyet ve sertlikti. Sonuçlarımız, aortik ark bölgesinin lokalize genetik modifikasyonunun embriyonun fizyolojisini yönettiğini ve dolayısıyla büyümenin sonraki aşamalarında KKH (doğuştan kalp hastalığı) gelişme riskini azaltacağını ve doğumdan sonra cerrahi müdahale ihtiyacını önleyeceğini gösterdi. Bu yaklaşım, konotrunkal bantlama ve civciv embriyosunun sol atriyal ligasyon modellerini içeren mekanik müdahale modelleri ile birleştirilebilir.

AKNOWLEDGEMENTS

بِسْمِ ٱللَّهِ ٱلرَّحْمَٰنِ ٱلرَّحِيمِ and ٱلْحَمْدُ لِلَّهِ

I would like to first and foremost acknowledge the teachings of the messenger of Allah, may peace be upon Him, which allowed me to break all socio-cultural norms and seek an education that would increase me in my knowledge and allow me to benefit from it. I would like to thank my professor for being the most supportive and encouraging presence throughout the course of my education, including the unexpected and unpredictable circumstances caused by covid. Without my Professor, Prof. Dr. Kerem Pekkan, I would not dare to dream and now, I not only dream but I know I can achieve these goals. I would like to thank my parents and siblings for being there for me from across many oceans. I would like to thank my friends who have helped me overcome the stress and pressure that inevitably comes during the course of an education. My lab mates who have been a constant source of relief for me and have helped me not only emotionally and mentally but even in my experiments and my writing. I would like to thank every presence in my life for the good and the bad which caused me to be where I am today.

TABLE OF CONTENTS

LIST OF FIGURES

CHAPTER 1

LIST OF TABLES

CHAPTER 1

LIST OF FIGURES

CHAPTER 2

LIST OF TABLES

CHAPTER 2

Chapter 1:Soft-Tissue Material Properties and Mechanogenetics during Cardiovascular Development

Introduction:

Embryonic cardiovascular development is an intriguing and vital process. This paper presents a comparative review of the material properties in the embryonic and fetal cardiovascular systems of different model organisms at consequent stages. An integrated and time-lapsed biomechanical and biochemical perspective of embryonic vascular re-modelling and vascular growth is central to this review effort. In addition, the signalling pathways that ultimately regulate mechanical properties of major components of the dynamic vascular phenotype are also revisited. Recent advances in embryonic animal models of altered mechanical environment and increasing access to the mRNA interventions also motivated this review. It is expected that targeted combination of both interventions will start to emerge in the literature. Furthermore, the material properties such as stiffness [1], stress–strain measurements [1], strain rate [2], and elasticity [3] enunciate the structural and functional properties of the cardiovascular system and can help identify the emergence of congenital heart defects (CHDs). Shear stress-responsive elements stimulated by blood flow cause cellular activities; hence, the study of resulting mechanical properties would also provide insight into the functional evolution of the developing system [4]. Critical functions such as apoptosis, organogenesis, epithelial-mesenchymal transition during heart-valve development, and associated gene expressions are influenced or directly caused by the mechanical stresses [5]. Elasticity plays a crucial role in the efficient pumping mechanics of the ventricles [6]. Mechanical factors such as myocardial wall stress and strain [7, 8], hemodynamic, and ventricular pressure [9-11] are also known to interfere with cardiac growth and development.

The stages of development of the embryo play a vital role in the targeted mechanical properties and their rate of change. System-level cardiovascular properties such as stiffness, compliance, and vascular resistance are significantly altered as the embryo develops [12]. While several empirical correlations have been drawn between the mechanical and morpho-structural properties of cardiovascular components [13], the properties are non-linear and, hence, require a foundation of soft-tissue mechanics and custom experimental tools [3]. The survival and sustainability during embryogenesis may require a tight balance between the hemodynamic parameters and material characteristics

[4]. Despite the overall changes during long-term development, some parameters such as stress–strain characteristics, stiffness, and stretch values tend to remain constant with growth, as demonstrated in key cardiovascular components [1]. Mechanical characterization is critical to detect cardiac anomalies with clinical significance at the early stages. An abnormality such as increased or decreased stresses, strains, or other mechanical factors can cause a fluctuation in the upstream transcription factors, which are indicative of the prevalence of cardiac defects [14-19]. Well-established transcription factors, such as KLF-2, ET1, and NOS3, are activated by wall shear stress [20-22]. Abnormalities in mechanical properties of the looping ventricle also have the potential to trigger CHDs [8, 23].

The biomechanics of cardiovascular development was initially investigated by a few pioneering research groups. Leading publications of these teams guided the present review systematics by providing the seed papers. Due to the authors' expertise and research interests, the recent experimental manuscripts published in specialized journals were screened from a biomedical and biomechanical engineering perspective. In this comparative review, for each species, we classified the cardiovascular system on the basis of its major components and compiled the embryonic stage-specific mechanical properties as they significantly change during development. The Carnegie stages (CS), a standardized 23-stage scale (up to 8 weeks of the human gestation period), are used as a scale to compare the embryonic development between different organisms [24].

The present review of embryonic mechanical characterization indicated gaps in literature where further experiments are needed. Therefore, two novel and non-invasive mechanical characterization techniques are introduced here for the first time in the literature. These techniques are applied to early avian embryonic stages and have the potential to address some of the experimental challenges discussed in this article.

The review starts with the basic methodology for measuring the material properties. The properties for avian embryos at key developmental stages are presented in detail due to the availability of ample data for this established cardiovascular animal model. Corresponding properties are compiled for porcine, human, and rat cardiovascular systems, in sequence. Despite the limited data and the complex/transitionary circulation system, Xenopus species are included for completeness [25]. The genetic impact of mechanical properties is reviewed, and the known interactions between the governing genes and morphology are presented. Thus, this review aims to establish insight into the

relationship among mechanical properties, morphological structure, and genetic characteristics of the cardiovascular system as it develops into its more complex and fascinating mature configuration across species.

2. Materials and Methods

2.1. Traditional Methods

Mechanical characterization includes basic mechanical testing and microscopic visualization, as summarized in Table 1. Experimental approaches include micropipette aspiration, optical stretching, optical tweezers, optical coherence tomography (OCT), micro cantilever-based techniques, pulsatile testing, and micro-indentation. These methods are used to observe mechanical factors such as stress-strain, elasticity, and strain energy function of soft tissues. The most popular and practical form of these techniques is tensile testing [13]. Tensile tests can be performed in a uniaxial or biaxial experimental setup to quantify the isotropic or anisotropic material properties of soft tissues, respectively [26-29]. However, they require the tissue to be extracted, and the quantification of small embryonic tissue properties locally via tensile testing is highly challenging, thus creating a niche for novel non-invasive methods.

Table C1 1: Summary of established mechanical techniques used to acquire the embryonic material properties and associated visualization methods.

Mechanical Methods and Numerical Models	**Ref.**	**Visualization Methods**	**Ref.**
Uniaxial/biaxial tensile testing	[1]	Optical coherence tomography	[2, 3]
Invasive/non-invasive residual stress experiments	[4]	Epifluorescence/fluoroscopy	[5]
In vivo pressurization	[6]	Microscopy	[5, 7]
Optical stretching and optical tweezers	[8]	Magnetic resonance imaging	[9]
Finite element modelling (FEM)	[10]	Echocardiograph	[11, 12]
Cantilever based technologies	[13]	Confocal/two-photon microscopy	[14]
Strain energy and Gasser-Ogden-Holzapfel models	[15]	Scanning electron microscopy	[16, 17]
Cuts	[18]	Histology	[19]
Micropipette aspiration with servo-null pressure measurements	[20]	Digital camera	
Beads	[21, 22]	Radiology	
Micro-indentation, atomic force microscopy	[3, 23]	Micro computed tomography	

To support the mechanical testing data, simultaneous visual observation of three-dimensional changes of the tissue microstructure is important. Quantitative visualization techniques include fluorescence microscopy, two-photon/confocal imaging, magnetic resonance imaging and echocardiography [34]. Some researchers, as in [47], incorporate optical microstructural tracking with mechanical testing such as uniaxial, biaxial, and multiaxial testing, for better inference. The samples are subjected to loading until complete rupture and the stress-strain curve/stiffness is acquired [13]. Developmental changes in material properties are best observed using advanced microscopy [42]. These techniques are often optimized for a specific tissue or target cardiovascular component [14]. Multiple methods are also employed simultaneously for cross-validation, as in [3]. For high-quality research data, in utero and in Ovo approaches are strongly preferred over the ex vivo or in vitro cultures of the developing cardiovascular components.

Due to the exponential nature of vascular stress-strain curves, the hyper-elastic exponential material model [48] is adopted to characterize the embryonic tissue [49, 50]. For example, the Ogden material model [51] is commonly used, as employed by Von Dassow et al. [52] and Yao et al. [8]to model Xenopus laevis embryonic tissue and looping heart tissue in chick embryo, respectively. A simplified form of the Ogden material model is the neo-Hookean strain energy function, which was used in our recent work to characterize the growth of aortic arch tissue at early embryonic stages of the chick embryo [45].

Another basic material model for mechanical characterization of the soft tissue is Fung's material model [53, 54]. Fung-type material is an anisotropic hyper-elastic constitutive model with the strain energy function described in [12]. Fung's equation represents a pseudo-elastic stress-strain relation (Equation (1)) and, thus, can be used to identify the corresponding nonlinear material parameters if the stresses and strains are experimentally evaluated.

$$\rho_o W = \frac{c}{2} expQ, \qquad (1)$$

where ρ_o is the mass density, W is the pseudo-strain energy per unit mass, c is a constant with a unit of kPa (stress), and Q is given by the following equation:

$$Q = b_1 E_\theta^2 + b_2 E_z^2 + b_3 E_r^2 + 2b_4 E_\theta E_z + 2b_5 E_z E_r + 2b_6 E_r E_\theta \qquad (2)$$

where Eo, Ez, and Er are Green's strain components in the circumferential, longitudinal, and radial directions, respectively, while b1, b2, b3, b4, b5, and b6 are the nonlinear material parameters and are constants for a given material. The values of bn correspond to the tissue structure, which determines the behaviour of the material, although an explicit physical mechanical parameter cannot be assigned to the constants. Most importantly, these material models can be implemented in finite element modelling (FEM) frameworks to solve the detailed stress/strain distributions in subject-specific computational models of developing cardiovascular components [55-58].

2.2. Novel Non-invasive Methods

The first non-invasive technique introduced in this manuscript simultaneously measures lumen diameter and pressure waveforms over the cardiac cycle using OCT (Thorlabs, Newton, NJ, USA) and a servo-null pressure system (WPI, Sarasota, FL, USA) respectively. These measurements are sufficient to estimate both the unloaded and the loaded Fung's material parameters. Furthermore, the residual stresses can be acquired noninvasively as demonstrated in our earlier work applied to mature arteries [12]. For developing tissues, residual stresses are critical as their hyper-restoration is presumed to drive vascular growth [59]. In the present paper, we applied this technique to characterize embryonic pharyngeal arches and the vitelline arteries of early avian embryo using fertilized Gallus gallus domesticus eggs for Hamburger-Hamilton (HH) stages [60] HH16 to HH24. This non-invasive data is presented for the first time in the literature. The experiments were conducted on five embryos to obtain the vitelline artery parameters and on eight embryos to obtain the IVth aortic arch vessel parameters, including their residual stress components and distribution. Since these experiments were conducted in Ovo, results include external mechanical effects from albumin, including surface tension, as the embryo is oriented close to the air sac.

Alternatively, as the next non-invasive approach, an actuator was used to create a wave of frequency in the range 0–20 kHz, as in tissue elastography [61]. A signal with a desired amplitude was generated and directed at the chick embryo in Ovo. A change in direction of the incident wave was observed in the OCT Doppler mode, depending on the local material properties the wave is reflected by. The change in the direction of frequency was recorded in the form of an image. Optimization of frequency and amplitude of the generated wave provided image data amiable for further analysis. The darker and lighter

sections in the image are representative of the material characteristics of the tissue. A preliminary experimental setup of this technique is provided in Figure C1 1.

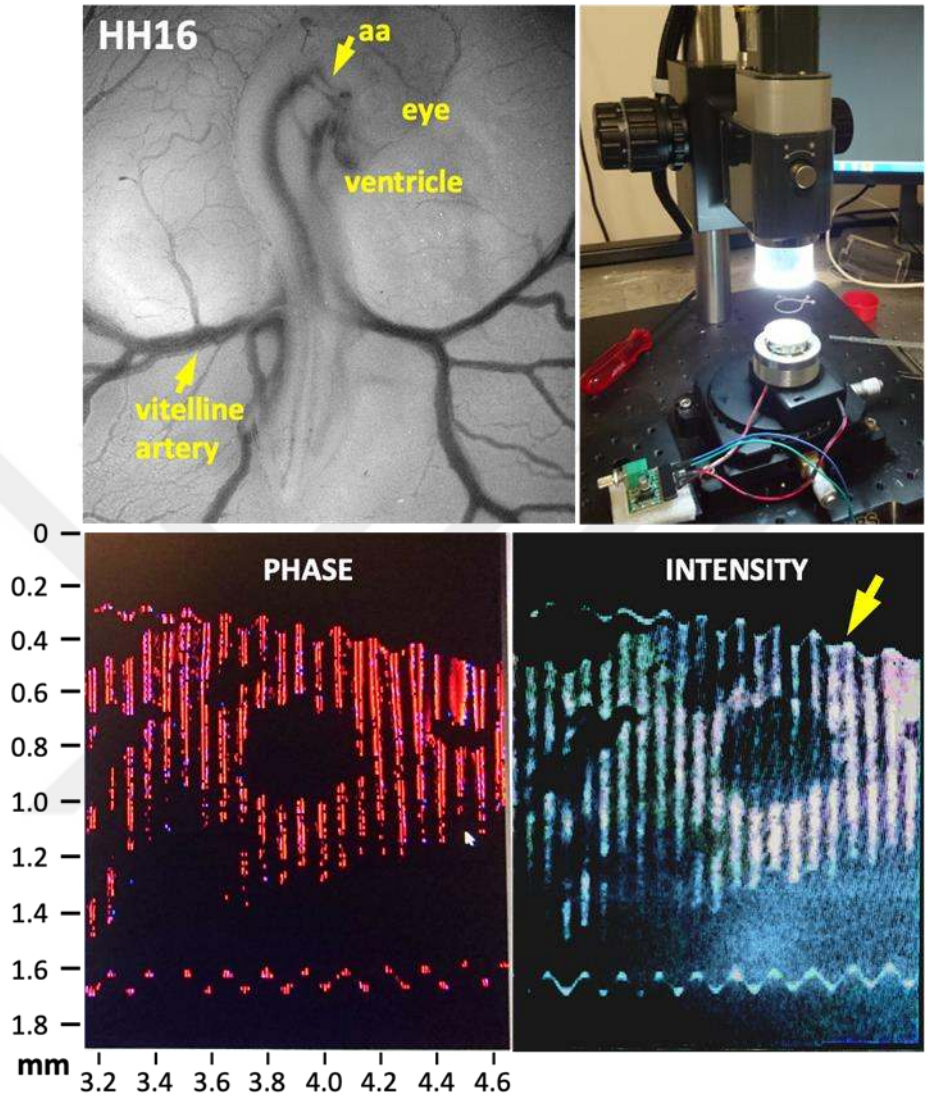

Figure C1 1: A. The experimental setup used to evaluate material properties in chick embryos at HH16 (vitelline artery) to HH24 (aortic arch, aa) is shown on the right. (A). Stage HH16 chick embryo imaged under a stereomicroscope is also provided. (B). Preliminary optical coherence tomography images of chick ventricle during acoustic forcing (0–20 kHz) per-formed for non-invasive elastography. A cross-section of the ventricle is displayed. The arrow points to the instantaneous deformation of the soft tissue.

3. Results

3.1. Avian Embryonic Development

Avian embryos, such as quail and chick, are the models of choice as they closely relate to the biventricular human cardiovascular system [62] and enable a large sample

size. In the literature, material properties have been studied for a broad range of embryonic HH stages and cardiovascular components, as summarized below.

3.1.1. Ventricles

Anatomical dimensions are first reviewed in order to provide an interpretation for the reported stress/strain levels and other mechanical properties. The left ventricle (LV) compact layer thickness, which excludes the trabeculations, is larger than that of the right ventricle (RV) from HH24 to HH34 [63]. Compact layer thickness is 45 μm and 35 μm at HH34 and HH24, respectively, for LV and 35 μm and 15 μm at HH34 and HH24, respectively, for RV. The total volume of the myocardium for a healthy embryo was observed to be ~0.7 mm3 and ~0.35 mm3 for the LV and RV, respectively, for combined compact and trabecular regions [63]. The LV wall thickness, including the trabeculae, is ~300 μm at HH27, and it progressively increases to ~440 μm at HH31 [63]. At HH29, the length of the RV and LV is approximately 1.25 mm and 1.75 mm, which increases to 3.5 mm and 5.5 mm at HH40, respectively [63]. Embryonic ventricular dimensions can also be estimated from published developmental atlases [64].

Earlier studies acquired the progressive changes in ventricular tissue strain values. For Leghorn chick embryo at HH16, micropipette aspiration was employed to measure the circumferential and peak axial Lagrange strain of the embryonic ventricle, indicating that the strains are different for systole and diastole, with the peak strain being -0.16 ± 0.08. There is a shortening of about 20% during systole [65]. Strain is higher near the boundaries of the primitive RV and reduces close to the mid-ventricle. Higher strain values imply potential for remodelling and enhanced biomolecular activity. The stiff myocardium supports the end-systolic pressure load indicated by the transmural stress distribution, accounting for the effects of residual strain. Residual stress levels significantly affect the stress distribution of the loaded state. For example, residual stress increases the stress concentration of the myocardial layer at HH17 [66]. For time-lapsed data, the non-invasive residual stress estimation approach introduced in Section 2.2 can also be applied to the ventricles.

At HH18, using uniaxial loading and FEM, the changes in the strain values between HH16 and HH18 were reported by Miller et al. [67]. The longitudinal Lagrangian strain of the ventricles was calculated from three microspheres at the top centre of the outer curvature and reached a maximum value of 0.19 at HH18. The cross-sectional area at HH16 was observed to be 0.049 mm2 and that at HH18 was observed to be 0.059 mm2

[67], indicating an increase in the thickness of the ventricles. An increase in strain indicates an improvement in the ventricles' capacity to withstand increased blood pressure during development. As the stages progress, the strain levels increase, as presented in Figure C1 2.

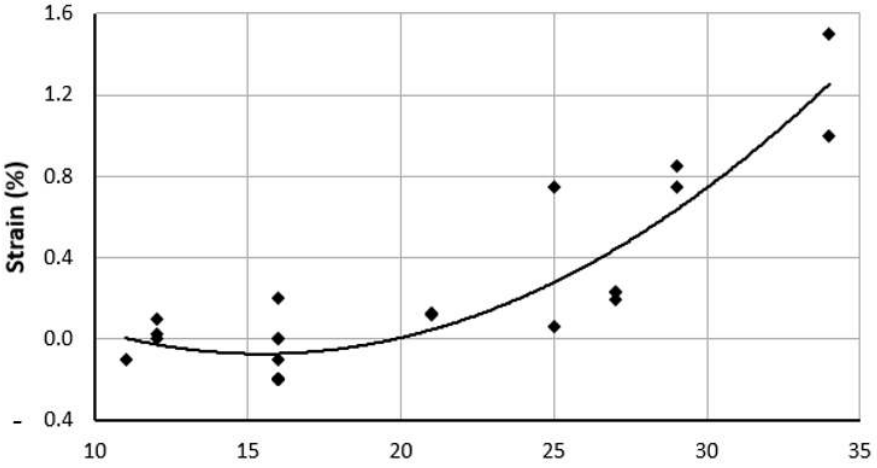

Figure C1 1: Overall strain trend of embryonic chick ventricles (LV and RV) presented as a percentage, as compiled from multiple literature sources, from HH11 to HH34. Corresponding references are cited in the text and in Table 2. HH: Hamburger-Hamilton stages.

Cyclic uniaxial loading of the LV shown by Miller et al. [67] at HH16 showed that the longitudinal strain ranges from 0.0 to 0.25, circumferential strain ranges from −1.5 to −0.01, and shear strain remains approximately zero. Thus, circumferential strains are negative, and longitudinal strains are positive. The thickness of the LV wall increases from 300 μm to 400 μm, from HH27 to HH31, respectively.

The conotruncal banding model (CTB) results in an acute increase in ventricular pressure leading to an abnormal development. Miller et al. [30] showed that when the LV of Leghorn chicks with CTB is subjected to biaxial loading, the stress/strain values remain unchanged from HH27 to HH31. This contrasts with the healthy LV development, for which these values decrease as the embryo develops, supporting the hypothesis that mechanical uniaxial loading primarily regulates the trabecular aspect [30]. Another study on the CTB model reported ventricular dilation, thickening of the compact myocardium and trabeculae, and spiralling of trabecular course in the LV [65]. Since the ventricle is an anisotropic material, strains evaluated along different axes result in different values. For this review, we report the circumferential strain while briefly exploring longitudinal strains. The circumferential strain is evaluated for a circular vessel from the inner radius to the outer radius. Values compiled from literature are summarized in Table 2, along

with their equivalent Carnegie stages, to allow for a timeline comparison across different species.

Tobita et al. observed the mechanical behaviour of ventricle strains at LV and RV measured for stages HH21 to HH31 [10], along the circumferential and longitudinal directions. Tobita et al. observed that the strain consistently increased with embryonic stage. Epicardial wall strain at end of diastole at HH11 and HH27 for the circumferential and longitudinal orientations at LV and RV was also reported [68]. As the embryo develops, strain increases linearly along all axes [69]. Table 2 summarizes the strain levels reported in the literature from HH11 to HH35. It is observed that LV consistently has a lower longitudinal strain than RV and a higher circumferential strain than RV [10].

Myocardial stiffness as an index of resistance to deformation, at stages HH21 and HH27, was measured by Tobita et al. [65] for LV and RV. The stiffness constant is a dimensionless quantity derived from the following equation: $\sigma = a \times \exp(bE)$ and reported for the normal embryo at HH27. The stiffness constant of RV is 4.5 and 5.4 circumferentially and longitudinally, respectively. The corresponding values of stiffness constant for LV are 7.8 and 9.6, in which the longitudinal stiffness is higher than circumferential stiffness [65]. LV is stiffer that RV due to reduced volume load compared to LV.

At HH24, the end-diastolic stiffness reported by Stekelenburg et al. [20] was 0.6 mmHg/μL for a healthy embryo. A decrease in passive filling is observed for stiffer ventricular walls. The relative weight of the embryo remains constant between HH12 and HH29. The effective elastance obtained from pressure–volume loops indicates the contractility of the heart. Contractility, defined as the ability of a muscle tissue to shrink, is estimated to be 7.53 mmHg/μL [20]. HH21 has a higher diastolic stiffness than HH24, indicating a decrease in stiffness and increase in elasticity as the embryonic timeline progresses. As expected, stresses differ during the contraction and relaxation phases of the heart; at the end-diastole, for HH21, it was measured to be between 15–20 mmHg, whereas, at end-systole, it is between 100–150 mmHg [69].

Strains are measured for the ventricles at the outer curvature, the centre, and the inner curvature for HH11 and HH12. While the microstructural properties are similar at the outer curvature and for the inner curvature, the circumferential direction has higher contractile stress levels. Strains at stages HH11 and HH12 are not significantly different

but are higher in the central region for HH11 along both cardiac axes [68]. Strain values compiled from the literature show an increasing trend, as displayed in Figure C1 2.

Ref.	Vascular Component	Parameter	Type	Stage		Value	Method
				HH	CS		
			Ventricle Looping				
[43]	ventricle looping	Pressure (kPa)	systolic	16	12.6	0.133	Computational model and cuts
			diastolic			0.033	
		Stress (kPa)	Cauchy			2	
		strain	max			0	
			min			−0.2	
			bending			−0.2	
			Epicardium				
[9]	epicardium	strain	max	16	12.6	0	epicardial beads
			min			−0.2	
			bending			−0.2	
		stress (kPa)	max			4	
		strain	max			−0.1	
			min			−0.2	
[68]	epicardial	strain	max circ	11	11	−0.1	triangular array
			max inner	12	11	0.1	
			systole bending	12	11	0.02	
			diastole bending	12	11	0	
			Ventricle				
[67]	ventricle	strain	max	16	12.6	0.2	MPA
[30]	LV	thickness (microns)		27	17.5	300	uniaxial and biaxial testing
				29	19	400	
				31	20	425	
[63]	LV	thickness (microns)	compact layer	24	16	30	Micro-indentation and FEM
				29	19	40	
				34	21	45	
	RV			24	16	40	
				29	19	60	
				34	21	70	
[10]	LV	strain	circumferential	21	15	0.12	Beads
				27	17.5	0.23	
			end diastole	21	15	0.12	
	RV		circumferential	21	15	0.13	
	RV			27	17.5	0.23	
	LV			27	17.5	0.19	
[7]	ventricle	pressure (kPa)	systole max	21	15	0.2	Cuts, theoretical model, and Micro-pressure system
			diastole max	21	15	0.067	
[70]			max	24	16	0.06	
[65]	myocardial	circumferential stiffness constant	RV	27	17.5	4.3	Beads
			LV	27	17.5	7.8	
[19]	LV	pressure	max diastole	29	19	0.631	

Table C1 2: Material properties of embryonic ventricles are summarized for the avian embryo. Regional properties of ventricles, epicardium, valve leaflets/cushions, atrioventricular region, myocardial wall, dorsal aorta, and atrium are compiled as available in the literature. Properties were evaluated at different embryonic stages primarily using the methods in Table 1.

Reference sources (Ref.) are provided in the first column. LV: left ventricle, MPA: micropipette aspiration, RV: right ventricle, CTB: conotruncal banding, LAL: left-atrial ligation, FEM: finite element modelling, AV: atrio-ventricular, CS: Carnegie stage.

Biaxial wall stress-strain relations also differ for the LV and RV as expected. Stress values peak at HH27 at any given strain level for both ventricles; however, for a CTB model, peak strain was observed at HH21 [65].

3.1.2. Heart Valves

For atrioventricular valve leaflets at HH25 to HH34, the corresponding strain energy density functions were provided in [49], by utilizing two different experimental approaches. Deformable cantilevers were used for stages HH25 to HH34, whereas micropipette aspiration was used for stage HH36. It was observed that the strain energy density of the leaflet at HH36 is four times that at HH34. The strain energy density was also observed to increase by a factor of 2.5 from HH25 to HH29. Along the embryonic leaflet, the superior cushion region had a strain energy density of 0.44 Pa, while the inferior had a strain energy density of 0.34 Pa. Mural strain energies were observed to change from 0.6 Pa to 0.9 Pa between HH29 and HH34, respectively. Other available values from the literature are provided in Table 2.

3.1.3. Aortic Arch and Vitelline Artery Properties

Geometry

Three paired aortic arch vessels appear in the development of early chick embryo. Wang et al. [73] studied the diameter of four of the six aortic arches and characterized the wall shear stress for these vessels. They observed that the midpoint diameters of the right arches are greater than the left and are in the range of 0.101 to 0.129 mm for HH18 and 0.113 to 0.138 mm for HH24, respectively [73]. Another study by Celik et al. evaluated the aortic arch diameters; at HH24, the maximum diameter was ~0.3 mm [74]. Lindsey et al. studied the diameter upon occlusion at HH18 and HH24 and found it to be ~0.2 mm [75].

Vascular Function, Pressure-Diameter Loops

In this section, employing the non-invasive approach described in Section 2.2 using pressure–diameter measurements acquired in vivo, a detailed mechanical analysis of vitelline arteries and the IVth aortic arch is presented. For both vessels, measurements indicate that the diameter increases nonuniformly with an increase in pressure (Figure C1 3). Another important finding is the existence of hysteresis during early stages as loading

and unloading cycles are significantly different. Further studies are needed to quantify the level of hysteresis during later embryonic stages and how it is probably reduced in relation to the microstructure.

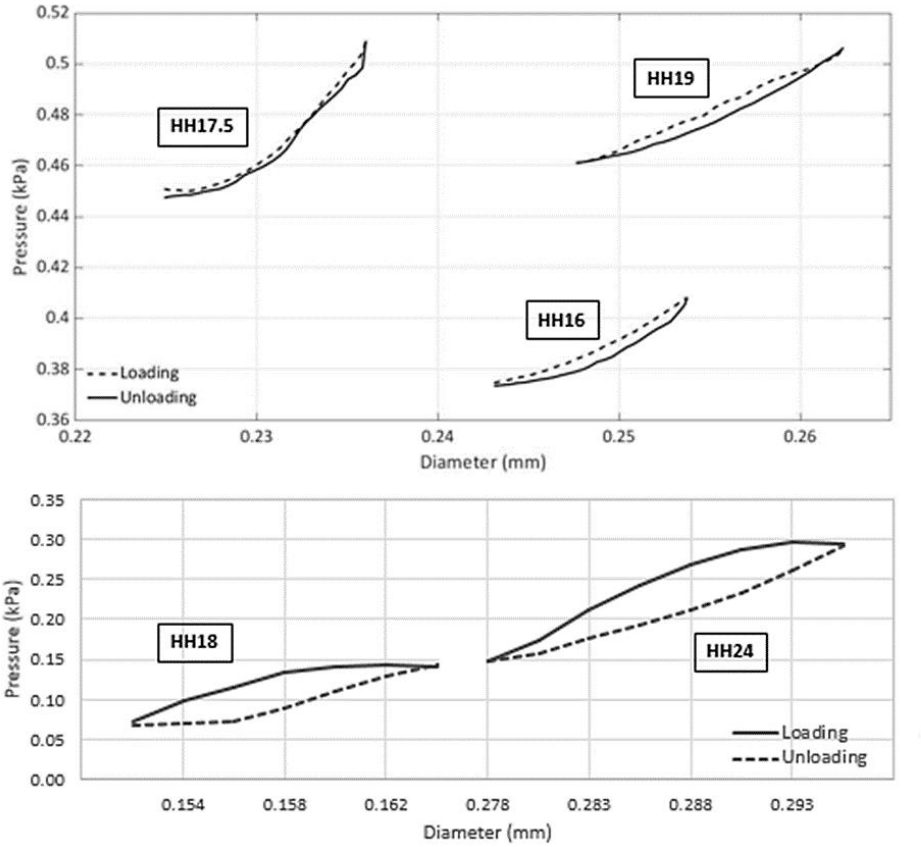

Figure C1 2: Representative pressure vs. lumen diameter loops of chick embryonic arteries acquired in vivo. (A). The vitelline arteries under loading and unloading conditions over the cardiac cycle. The data were collected for eight embryos (one representative sample shown) at three consequent stages of HH16, HH17.5, and HH19. (B). Right IVth aortic arch loading and unloading data over the cardiac cycle. The data were collected for five embryos (one sample shown) at two consequent stages of HH18 and HH24. Other sample data are available in the Supplementary Materials, and statistics are provided in Table 3. Data were acquired simultaneously using OCT and the servo-null pressure system described in Section 2.2.

Pressure-diameter loops and the vessel thickness change during the cardiac cycle were used to obtain the Fung's strain energy constants for both arteries using the method introduced by Donmazov et al. [12]. The values for the constants from Equation (2) were calculated and are presented in Table 3.

	Vitelline Artery ($n = 5$)								Aortic Arch ($n = 8$)			
	Loading				Unloading				Loading		Unloading	
HH	16	17.5	19		16	17.5	19		18	24	18	24
c	0.46 ± 0.03	0.51 ± 0.04	0.58 ± 0.04	*c*	0.43 ± 0.03	0.47 ± 0.04	0.57 ± 0.04	*c*	0.51 ± 0.03	0.61 ± 0.07	0.48 ± 0.02	0.57 ± 0.06
b1	4.68 ± 0.14	4.45 ± 0.14	4.23 ± 0.13	*b1*	4.49 ± 0.14	4.14 ± 0.13	4.1 ± 0.12	*b1*	6.51 ± 0.19	5.00 ± 0.25	6.09 ± 0.18	4.68 ± 0.24
b2	2.81 ± 0.14	3.12 ± 0.15	3.28 ± 0.16	*b2*	2.69 ± 0.13	2.91 ± 0.14	3.18 ± 0.15	*b2*	2.53 ± 0.07	2.13 ± 0.07	2.37 ± 0.07	1.99 ± 0.07
b3	0.65 ± 0.02	0.67 ± 0.02	0.65 ± 0.02	*b3*	0.63 ± 0.02	0.62 ± 0.02	0.63 ± 0.02	*b3*	0.63 ± 0.05	0.59 ± 0.06	0.59 ± 0.05	0.55 ± 0.05
b4	0.37 ± 0.03	0.45 ± 0.04	0.51 ± 0.04	*b4*	0.36 ± 0.03	0.42 ± 0.03	0.50 ± 0.04	*b4*	0.32 ± 0.02	0.27 ± 0.03	0.30 ± 0.02	0.26 ± 0.03
b5	6.04 ± 0.14	7.07 ± 0.17	7.86 ± 0.19	*b5*	5.80 ± 0.14	6.58 ± 0.16	7.62 ± 0.18	*b5*	6.40 ± 0.12	5.11 ± 0.12	5.99 ± 0.11	4.77 ± 0.11
b6	1.47 ± 0.03	1.76 ± 0.04	1.86 ± 0.04	*b6*	1.41 ± 0.03	1.64 ± 0.04	1.81 ± 0.04	*b6*	0.98 ± 0.03	0.90 ± 0.03	0.91 ± 0.03	0.84 ± 0.03

Table C1 3: Estimated Fung's strain energy function parameters (Equation (1)) for loading and unloading at HH16, HH17.5, and HH19 for the vitelline artery vessels and for the IVth aortic arch at HH18 and HH24 are tabulated. Sample numbers (n) are indicated for each artery type.

Vitelline artery: As presented in Table 3, the constant c is related to residual stress and increases with the stage of the embryo, as expected from pressure measurements and opening angle data. Constant b1 decreases as the embryo develops, and b3 nearly remains constant, while all other parameters (b2, b4, b5, and b6) increase during the growth of the vitelline artery. Due to in vivo measurements, a slight irregularity in loading curves is recorded. These parameters were evaluated under loading and unloading conditions. For example, it is observed that the constant c displayed a similar trend for both conditions, although the increment was steeper for loading. All other parameters had a similar trend for both loading and unloading conditions from HH16 to HH19.

Aortic arch vessels: Aortic arch vessels behaved differently as compared to vitelline artery during growth. The calculated Fung's strain energy function parameters were similar for each stage, confirming the calculations noted in Table 3. The constant c increases with stage, b3 and b4 are nearly constant, and b1, b2, b5, and b6 decrease as the aortic arch grows. When these parameters were observed during loading and unloading conditions, parameter c followed the same trend for both with a steeper increase during loading. All other parameters had a similar behaviour during both loading and unloading.

Effective Opening Angle and Residual Stress

Effective opening angle is derived from the loaded and unloaded ventricular morphology, as employed in the experiments conducted by Taber et al. on embryonic chick ventricles at HH stages 16, 18, 21, and 24 [69]. The effective opening angle increases as the stiffness of the vessel increases (31° at HH16), which is the residual stress component in one direction. Residual stress components along the orthogonal directions require additional incisions for the invasive approach. For the micron-size embryonic arteries, these experiments are very challenging to perform. As an alternative, herein, we present the results obtained from our non-invasive measurements based on Donmazov et al. [12].

Supplementary Figures S1 and S2 show the measured embryonic residual stress trends through the vessel wall along the radial (r), longitudinal (z), and circumferential (θ) directions. Residual stresses were computed for the vitelline artery and for the IVth aortic arch. It was found that, for the increased loading condition, residual stresses are greater than for unloading for both vitelline artery and aortic arch. In addition, an increase was observed in the values of residual stresses as the vessels grow.

Vitelline artery: As plotted in Figure C1 4, it can be concluded that the vitelline artery at HH19 is stiffer than at HH16. Moreover, the sharp increase in its effective angle from stage HH17.5 to HH19 confirms this finding. Axial residual stress increases from 0.3 kPa to 0.4 kPa between the stages HH16 and HH19. The increase in residual stress in the circumferential direction and the radial direction is similar (~0.5 kPa).

Aortic Arch vessels: Vessel stiffness also increases for the IVth aortic arch from HH18 to HH24 (Figure C1 4). The effective angle is higher during the loading condition and agrees with the stiffness trend. Results indicate that the increase in axial residual stress for aortic arch vessels is much higher than the increase for the vitelline artery. The residual stress in axial direction at HH24 is almost twice the residual stress at HH18. While circumferential residual stress is 0.17 kPa at HH18, it almost doubles and becomes 0.33 kPa at stage 24. Although the increase in radial direction is not as high as in other directions, there is about a 0.1 kPa increase between the two stages studied [45].

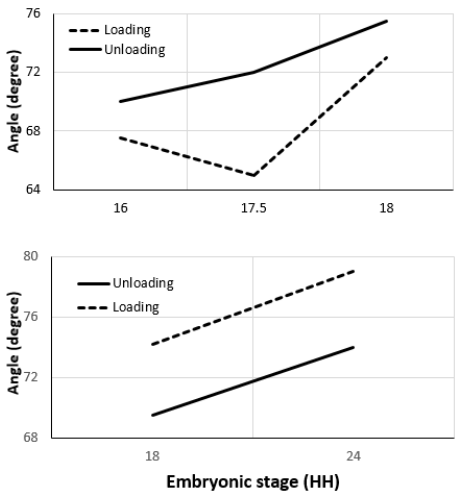

Figure C1 3: Changes in the effective opening angles of chick embryo arteries during early development are plotted. (A). Opening angle for vitelline arteries at stages HH16, HH17.5, and HH19 during loading and unloading conditions. (B). Opening angles for IVth right aortic arch at stages HH18 and HH24. Plots represent typical data collected over 13 chick embryos. Opening

angles were calculated in our lab using the methodology presented in [12] using OCT and servo-null pressure data.

Supplementary Figure S3 highlights that stress values are variable through the vessel wall and that the stress-strain relation is incremental. Both the vitelline artery and the aortic arch have the same characteristics in terms of residual stress distribution for loading and unloading conditions. Residual stress in the axial and radial directions increases from the inner vessel wall to the outer vessel wall, contrary to circumferential residual stress, which decreases.

Stress Distribution and Anisotropy

In the literature, ample information is provided for flow-induced wall shear stresses [76]; however, tissue stresses derived from Fung's equation are unique to the present review as these values require a comprehensive structural soft-tissue analysis. As a general trend, stress increases with the growth of the vessel, and the slope of the stress–strain curves indicates slight stiffening. For both the vitelline artery and the aortic arch, the slopes of the stress-strain curves are higher for embryos at the later stages of development. As the embryo develops, it has increased circumferential rigidity compared to younger embryos. The von Mises stress distribution through the vessel wall is similar for relatively close stages. It is lowest at the inner wall of the vessel and highest at the outer wall for both vitelline and aortic arch vessels.

Vitelline artery: The von Mises stress at HH16 lies in the range of 0.17 to 0.22 kPa between embryos. For stages 17.5 and 19, the von Mises stresses are almost equal, in the range of 0.21 to 0.26 kPa. The von Mises stress is larger for loading than the unloading condition at all stages. Loading and unloading conditions have similar trends for von Mises stress values; however, HH19 has a higher von Mises stress than HH17.5.

Aortic arch vessels: At stage HH18, a large variation in stress values is recorded, ranging from 0.12 to 0.2 kPa and from 0.2 to 0.28 kPa for unloading and loading conditions, respectively. Stress values at HH24 are much higher than at HH18. The von Mises stress at HH24 lies in the range of 0.45 to 0.7 kPa.

3.2. Large Animal Models

For completeness, basic anatomical dimensions are first reported. In sheep, LV thickness at 80 days of gestation period is 2.2 mm, while, at day 127, it increases to 3.1 mm. When an artificial aortic banding was employed surgically, it was found that the thickness remains the same initially but increases significantly at later stages of

embryonic development (7 mm at 140 days of gestation) [77]. The mitral valve diameter of the ovine foetus at 100 days of gestation is reported as 9.1 mm, while the aortic valve aortic annulus is 6.44 mm. An increase in the mechanical loading results in an increase in the mitral valve dimensions but a decrease in the aortic annulus [78].

Embryonic data on biomechanical properties of bovine and ovine cardiovascular components are limited. Despite the ample biomechanical data on mature porcine heart valves [28, 79-82], limited embryonic studies have been conducted to our knowledge. Ovine arterial pressure at the fetal stage was measured for different gestational ages. While the mean aortic blood pressure in the first week of gestation is 2.5 mmHg [78], 5 weeks after gestation, it reaches 25 mmHg. At 116 days of gestation, the fetal descending aortic blood pressure is 41.1 mmHg [83, 84] and the right-atrial pressure is ~2 mmHg, 115–121 days after gestation [83]. At the same gestational age (fifth week of gestation), the descending aortic blood pressure was found to be 64 mmHg [85]. The aortic pressure of the ewe was found to range between 39.2 and 41.0 mmHg, 126 days after gestation. Mean arterial pressure (MAP) remains nearly constant as the embryo develops; however, if there is an increased systolic load (40 mmHg for 8 days), the mean arterial pressure increases to 63 mmHg in 8 days [86]. A study conducted in 1989 measured the fetal blood pressure in ovine models to be ~44 mmHg [87], but no stage information was provided.

In [13], fetal and adult mitral valves were compared, where the maximum stress was observed to be 0.36 MPa for fetal porcine mitral valves (third trimester) and 1.48 MPa for 10 day old porcine mitral valves (Table 4). As the foetus develops, the thickness, the modulus of elasticity, and the stresses increase, as presented in Table 4, correlated with increased collagen content [13].

Porcine						
Ref.	**Organ**	**Parameter**	**Stage**	**CS**	**Value**	**Method**
[13]	Mitral valve leaflet	thickness (mm)	Third trimester	-	0.4	uniaxial tensile testing
		stress (kPa)			7000	
		strain			0.35	
		ultimate stress (kPa)			0.400	
		modulus of elasticity (kPa)			200	

Rat						
Ref.	Organ	Parameter	Stage		Value	Method
			ED	**CS**		
		Ventricle				
[88]	Ventricle	Systolic pressure (mmHg)	10.5	7	3	Pulsed Doppler velocimetry and Micro pressure system
			11.5	8	5	
			12.5	9	6.5	
			13.5	10.5	8.2	
	LV	End diastolic area (mm^2)	11.5	8	0.77	
	RV		11.5	8	0.77	
	LV		12.5	9	0.8	
	RV		14.5	11.5	1.29	
		Cardiac Myocyte				
	cardiac myocyte	Pressure (N/m)	2 days	-	0.75	
		Xenopus				
[35]	myocardium	Stiffness (kPa)	48 hpf	-	10	FEM, cannulation, and pressurization
[89]	Heart tube	circumferential stress (kPa)	24–30 hpf	-	7	Computational

Table C1 4: Summary of the material properties for swine, rat, and Xenopus models during embryonic development. Embryonic stages for mice are recorded using the ED scale (embryonic day). ED0 is the day of fertilization, followed by ED1, ED2, etc. Similarly, for Xenopus, a scale measuring the number of hours post fertilization is used. As a general reference, CS is also provided. LV: left ventricle, RV: right ventricle, CS: Carnegie stage, ECG: electrocardiography, hpf: hours post fertilization.

Cellular-level mechanical characteristics have been reported for large animals in the literature. Mononucleated and binucleated myocytes exhibit different lengths in ovine foetuses. At 135 days of gestation, mononucleated monocytes are 65 microns in LV and 69 microns in RV, with a width of 12 and 13 microns, respectively. Binucleated myocytes, on the other hand, have a length of 84 microns in LV and 92 microns in RV with a similar width to mononucleated myocytes [77]. Cardiomyocytes are generally unaffected by a reduction of load, but hyperplastic growth is affected by a reduced load in developing fetal hearts, as shown by a study conducted over a 100 day gestation period [78].

3.3. Human Embryonic Development

A reasonable estimate of human embryonic vascular properties can be obtained from umbilical vein and arteries. Maximum strain and stress values of the umbilical vein are 6 and 2.85 MPa, respectively [3]. The Young's modulus and maximum stress were calculated to be 2.18 and 6.01 MPa, respectively. Since the umbilical tissue is anisotropic, an average global strain value is calculated over the complete region, which peaked at −14.4% for RV and −13.8% for LV [90]. As the foetus ages, the peak strain reduces. For instance, the LV strain increases from −13.8% in the first trimester to −10.8% in the second trimester. It is also observed that the LV strain is higher than the RV strain in the first trimester, but the RV strain is higher in the second trimester.

Throughout gestation, the global longitudinal strain decreases while the strain rates remain unchanged. The LV attains a higher strain value than RV with a mean value of 28% and 26%, respectively. The globally averaged longitudinal strain rate is 3.12 and 3.37 for RV and LV, respectively. A linear relationship can be developed between the gestational age and maximum strain [38].

Stress–strain characteristics measured in the radial direction for the umbilical vein show that, with the increase in artery wall thickness, the radial tensile strength increases until 750 μm, where the corresponding tensile strength is 7.5 N (Table 5) [42]. Similarly, the strength at 250 μm is 6 N, which implies that a lower thickness corresponds to lower stresses. Longitudinal tensile strength shows the same trend between 250 and 750 μm with values ranging from 9 to 21 N.

Another measure for estimating the material properties is by comparing the point of failure. In uniaxial or biaxial tensile testing, the material is stretched until failure which gives insight into the strength, elasticity, and stiffness of the material. Failure is caused either by direct and known stresses (primary failure) or by indirect, unknown stresses in the environment (secondary failure), both of which contribute to understanding the viscoelastic properties of the material. As an example, the umbilical cord consists of a component called the ringlet, as investigated by Rodriguez et al. [42]. Ringlet secondary failure occurs at a stress value of 0.5 MPa and remains constant as the thickness increases and the embryo develops However, the ringlet primary failure occurs at a higher stress value (2.1 MPa) for a lower umbilical arterial thickness and at a lower stress value (~0.4 MPa) as the thickness increases to 1000 μm. Similarly, longitudinal failure is highest at

250 μm at 3.4 MPa and lowest at 1000 μm. This shows that, as the embryo develops, it becomes stiffer and fails under lower stress values (Table 5).

The longitudinal tensile strength of the umbilical artery is the greater than the circumferential values (Table 5). The suture retention strength, as shown by Rodriguez et al., of the umbilical artery is highest (1.75 N at 1000 μm) and increases with increased thickness, as expected. Burst pressure evaluates the ability of a vessel to withstand high blood pressures. For the umbilical artery, the highest burst pressure is sustained at 1000 μm wall thickness, with a value of ~1500 mmHg [42]. Although the ability of the artery to withstand high pressure increases with thickness of the vessel, it decreases at a thickness of 750 microns to a value of 1250 mmHg. Umbilical cord arteries, however, were surprisingly found not to have any significant changes in the mechanical properties with an increase in gestational age [1]. Umbilical strain is a measure of deformability of the artery without any permanent deformation with respect to the original length. Although the strain increases with time, it is highest at the 30th week with a value of 1.52 [1].

Ref.	Organ	Parameter	Type	Stage (Weeks)	Value	Method
			Myocardium			
[90]	myocardium	strain (%)	RV global	1st trimester	14.4	Uniaxial tensile testing, FEM, and ECG
			LV global		13.8	
			RV regional		13.9	
			LV regional		13	
			Ventricle			
[38]	LV	strain (%)	global	16–21	28.6	ECG
	LV			22–27	27.47	
	LV			28–38	26.61	
	RV			16–21	27.79	
	RV			22–27	26.48	
	RV			28–38	24.72	
	LV		systolic	21	−15	
	LV			28	−25	
	LV			34	−35	
			umbilical vein			
[3]	umbilical vein	strain	derived from true stress and/or strain	-	4.1	FEM and uniaxial tensile testing
		elastic modulus (MPa)			4.5	
		stress (kPa)	max		6000	
		strain	max		0.9	
			umbilical artery			
[1]	umbilical artery	stiffness (kPa)		25	57.89	uniaxial tensile testing and scanning electron microscope
				26–30	55.51	
				31–35	76.53	
				36–40	80.83	
		strain		25	1.33	
				26–30	1.52	
				31–35	1.39	
				36–40	1.41	
[42]		burst pressure (kPa)		-	200	
		strength (N)	suture retention	-	1.75	
		stress (kPa)		-	3500	
		strength (N)	longitudinal tensile	-	21	
		strength (N)	radial tensile	-	8	
			Aorta			
[39]	aorta	Stiffness index	aortic compliance	25	0.7	
				30	0.5	

Table C1 5: Basic properties of human cardiovascular components at different gestational ages. Clinical measurement techniques and clinical image modalities are generally employed for data acquisition.

3.4. Small Animal Models

For mice, the stages of embryonic development are defined in embryonic days (ED). Experiments conducted by Ishiwata et al. [88] for the end-diastolic area showed that the values increase as the embryo develops. At embryonic day 11.5 (ED11.5), the area of the LV and RV was found to be 0.77 mm2. The area increased from 0.8 mm2 at ED 12.5 to 1.29 mm2 at ED 14.5 [88].

Nonlinearity in the LV stiffness trend due to preconditioning behaviour of resting myocardium is explained by strain softening [92]. Wistar–Hannover rats showed lower circumferential strain (−24.8%) than longitudinal strain (−19.3%). Pulmonary congestion resulted in higher longitudinal strain at about −10.1% and −13.8% circumferentially. Global strain rate showed a similar trend with circumferential and longitudinal strain rates of −4 s−1 and −4.7 s−1, respectively [93].

Alterations in myocardial stress and strain at septal walls reduce the functional capacity of the ventricle. These abnormal changes may indicate the presence and severity of CHD, as seen in Table 6. For example, myocardial strain levels for a heart with fibrotic infarction progressively increase to nearly twice the strain values of a healthy heart [14]. Table 6 reviews additional clinical cardiac abnormalities with significance in material properties.

Fetal Malformation	Change in Material Property	Ref.
Fibrotic infarction	Doubled ventricular strain and increased myocardial stress.	[14]
Conotruncal defects	Increased ventricular pressure	[19]
pulmonary congestion	Higher longitudinal strain compared to the circumferential direction	[94]
Hypertensive heart	Increased stiffness	[15]
	Reduced strains in LV	[16]
	Reduced systolic strains	
Hypertrophy	Increased ventricular wall thickness and stiffness	[17]
aneurysm	Higher end diastolic stresses and cross-fiber stresses	[18]
Marfan syndrome	Enlargement and weakening of heart muscles	[95]
Loeys-Dietz syndrome	Enlargement of aorta	[96]
Ehlers-Danlos syndrome	Reduced elasticity, strength, and stiffness of the aortic vessels	[97]
Fibrotic infarction	Decreased ventricular pressure with compact and thinner myocardium	[19]

Table C1 6: General material property trends for selected cardiac malformations. CTB: conotruncal banding, LV: left ventricle, RV: right ventricle, CHD: congenital heart disease.

Stresses were calculated for various cardiac regions, and it was seen that, when a fixed load is applied during uniaxial tensile testing, the circumferential, longitudinal, and radial stresses increase from 2.8 to 18.2 kPa, 1.5 to 9.7 kPa, and 0.1 kPa to 0.6 kPa,

respectively. The increase in stress is 10-fold. Corresponding strain levels also increase from 0.100 to 0.138. RV deformations affect the LV diastolic mechanism and LV passive inflation. For both ventricles, stresses vary for the basal, equatorial, and apical and for the anterior, lateral, posterior, and septum regions. The highest stress is observed at the lateral equatorial region, reaching 3 kPa [98].

3.5. Mechanogenetic Regulation and Response

Vascular material properties are regulated through specific genetic pathways. In particular, the timescales involved in this tightly coupled system are not well established. In addition to the direct synthesis of matrix constituents, genes program material properties through biochemical means such as paracrine pathways to ensure that the cardiovascular system remains in its optimal condition. Cardiac looping and left–right asymmetry in ventricles are physiological features that are regulated by genes and play a role in the CHD and cardiac development [99]. Cyclic strain also plays a major role in cardiomyogenic differentiation of rat bone marrow stem cells as opposed to shear stress, and it increases cardiomyocyte-related markers [100].

The effect of shear stress has been studied in avian and mice embryos in the cardiovascular systems (umbilical arteries, and veins). It was observed that the gene expression profiles are altered by a shear stress-initiated release of prostacyclin and NO. Activated by changes in wall shear stress values [21, 22, 101-106], well-established mechanosensitive genes such as ET-1, NO, and eNOS are integral parts of the cardiovascular system. Growth hormone ET-1, for instance, is involved in vasoconstriction, and NO is involved in vasodilation [21], while KLF-2 is involved in vasculogenesis and angiogenesis [107]. Fluid shear stress is known to suppress endothelin 1 mechanosensitive genes [108]. ET-1 inter-acts with elastin and alters calcium content [109-112]. Elastin (Eln) in porcine embryos was evaluated, and its expression intensity was 42 in the third trimester. Despite the obvious differences in mitral and aortic valves following birth, these valves are identical in their genetic composition at the embryonic and fetal stages [113].

It is well established that arterial endothelial NO production and eNOS expression are controlled by shear stress [106]. KLF-2 expression is highest where the stress is highest. When the regulation of these genes is affected due to an inconsistency in the shear stress levels, the genetic risk factors for CHD increase, as in the NOS expression regulated by fluid shear stress [22, 101]. Another study showed that the nature of force

experienced influences the response of the endothelial genes [114]. Shear stress increases eNOS mRNA levels and cyclic stretch affects ET-1 mRNA levels. When applied simultaneously, the response of genes is significantly different from the individual effects.

Cardiac load also affects several genes and their expression levels. When the cardiac load is increased, a significant difference is observed in the levels of Notch-1, TGF-2, Wnt-2b, and BMP-1. For both mitral and aortic valves, these levels decline with the increase in load. Similarly, mRNA expression levels of elastin, type I collagen, and versican all decrease [115]. Cardiac malformations are known to depend on TGFβ levels [116] and shear stress affects KLF2 levels by activating the TGFβ/ALK5 signalling pathway [103, 116, 117]. In particular, miR-1 affects structural remodelling of the heart [118]. miR-128 regulates hyperplasia and Islet1 expression levels during cardiac regeneration [119]. Other genes such as Cadherin-11 and Fibirillin-1 affect thickness and arterial diameter. These genes also affect the calcification pathway in the cardiovascular system [120, 121]. AGTR1, ACE, AGT, CYP11B2, and ADD1 are some factors that affect elasticity in the system [105]. MMP3, MMP9, and M235T affect the stiffness and impedance through the activation of factors. NFκB, MAP Kinase, MEK, and PI-3K affect the shear stress response in the system [31, 122, 123]. SMAD6 is indirectly associated with the thickness of the aorta despite not being mechanosensitive [124]. As such, abnormalities in SMAD levels can cause thoracic aortic aneurysms. The plasticity index is monitored by PKP2 in cardiac cells. Stress also activates IL33, which plays a role in end-stage cardiac failure [125, 126]. RAAS is another important gene which is reported to influence the stiffness of the cardiac vessels [127]. Table 7 presents the mechanosensitive and mechanoresponsive genes that have been studied in literature.

Gene	Organ	Defect	Mechanosensitive	Indirect Alterations	Mechanical Properties Altered	Ref.	GP
Fibulin 4 coded by EFEMP2 gene	Large conduit arterial walls in mice	Ascending Aortic aneurysms, loose skin, bent forelimb, tortuous artery, and pulmonary emphysema	Interacts with elastin directly	-	Alters elastin, binds to calcium	[109] [110] [111] [112]	KI KO KI KO
Endothelin 1 (ET1)	Human umbilical vein endothelial cells		Reacts directly to shear stress and cyclic stretch		Shear stress and cyclic stretch	[114]	WT
Elastin coded by Eln	Mouse aortic walls	Arterial stenosis, hypertension	Direct interaction	-	Alters elastic fibers, thickening and arterial tortuosity	[110] [128] [129]	KO M KO
miR-1	Cardiac contractile function in mice	Damage in sarcomere assembly	-	Targets UTRs of MYLK3, CALM1, and CALM2	Affects structural remodeling of the heart	[118]	KO
VEGF	Endothelial cells	Matrix stiffens	-	In turn effects MMP activity	Stiffness, intima	[104, 130]	M
Cadherin-11	ECM in aorta in mice	Cardiac dysfunction in valves	-	Reduced Sox9 activity, β1 integrin expression, and RhoA-GTP	Increases thickness and alters stress fibers, causes calcification	[120] [121]	KO KI
Fibirillin-1	Mice arteries	Mutation causes Narrowing			Affects arterial diameter	[128]	M
NOS-3, KLF-2, ET-1 (can be altered by changing trichloroethylene doses) [131]	Chick, bovine, mice embryonic cardiovascular system		Shear stress induced	KLF2 indirectly activated by TGFβ	Activated by shear stress	[104] [101, 106]	M WT
TGFβ	Embryonic endothelial cells (human)	Cardiac malformations	Activated by shear activities	Can be affected by fibulin deficiency	Directly activated by shear stress	[103, 116, 117]	WT, M
ROBO4	Bicuspid aortic valve and thoracic aortic	CHD and aneurysm				[132]	KO
Notch1	Mice aorta	Ascending Aortic Aneurysm				[133]	KO

AGTR1, ACE, AGT, CYP11B2, ADD1	Human artery, vascular	CHD		Indirect association	Elasticity	[105]
MMP3, MMP9, M235T	Human artery, mice vascular	CHD		Indirect association	Stiffness and impedance	[105, 134]
NFκB	Vascular response in mice		Direct		Activated by shear stress	[123]
MAP Kinase	Blood vessels		Shear activated or stretch activated		Shear stress and stretch	8
MEK, PI-3K	Ovine fetoplacental artery endothelial cells			Activated by eNOS (indirectly activated by stress)	Shear stress	[31]
SMAD6	Thoracic aorta and bicuspid valve in humans	Thoracic aortic aneurysm		Indirect	Thickness	[124]
PKP2	Cardiac cells in Mice			Indirect, affects miR200b first	Knockdown causes reduced stress and work of detachment, increases plasticity index	[135]
IL33	Myocardium in mice and humans	Failing heart	Induced by mechanical stress		Stress	[126] [125]
miR-128	Cardiac ECM	Hyperplasia		Regulates hyperplasia and Islet1		[119]
RAAS	Cardiac vessels	Vascular hypertrophy		Regulates stiffness	Stiffness	[127]

Table C1 7: Mechanical property phenotypes and the response of mechanosensitive genes that play a critical role in structural cardiovascular development are summarized. Mechanosensitive genes are activated as a response to mechanical changes, while mechanoresponsive genes cause a mechanical change in the tissues. The effect of abnormal gene/pathway signalling is associated with cardiovascular system defects. WT: wild type, KO: knockout. KI: knock-in, M: mutant, R: review

4. Discussion

Among the several vascular components reviewed here, the myocardium has the highest stress concentrations at end-systole, while the residual stresses are responsible for further augmenting this stress level. At the early embryonic timepoint, the cardiac jelly present between the myocardium and the endocardium helps to enhance systole and diastole. Similarly, the stresses of the RV and LV are nonuniformly distributed at later stages [9]. As the embryo matures from HH16 to HH18, a 0.01 mm2 increase in the cross-sectional area of the tubular ventricle is observed. The LV cross-sectional area also increases from HH27 to HH31, together with the ventricular strain due to increased stress levels [67]. It was found that the LV is always thicker than the RV [63]. Similarly,

ventricular length increases with development. The strain data show a similar trend for the ventricles [30]. Later stages experience lower stress levels in the ventricles between HH21 and HH27. It was also observed that circumferential strain is always higher than longitudinal strain [68]. RV has lower myocardial stiffness than the left in all cases and in all directions [65]. Compact layer thickness also increases as the chick embryo matures. This layer carries the highest stresses corelated with growth. Systolic pressure is significantly lower than diastolic pressure. Likewise, diastolic stiffness is also higher than systolic values. However, the diastolic stiffness reduces as the embryo develops [9, 68, 69].

Strain energy for developing septal heart valve leaflets increases as the embryo develops. The superior cushion of the heart valve leaflets experiences higher strain energy than the inferior. Myocardial mural strain energy also shows a similar increase with the embryonic development.

Longitudinal strength and suture retention strength for the umbilical arteries increase uniformly with the increase in thickness, while burst pressure increases nonuniformly, as shown by Rodrigue et al. [42]. It is also seen that, as thickness increases, primary and longitudinal failure occur at lower stress levels unlike secondary failure, which remains nearly constant.

While the mechanical properties of disease states were not the focus of this review, it is well established that the symptoms of fibrotic infarction include nearly doubled ventricular strain and increased myocardial stress [14]. Mechanical interventions and diseases can lead to similar effects. For example CTB shows increased pressure in the LV [19]; thus, we can conclude that conotruncal cardiac anomalies also cause increased pressure in the LV. As such, pulmonary congestion occurs when the longitudinal strain is higher than circumferential strain. Reduced strains in LV [16] and systolic strains [15], as well as increased stiffness [16], cause a hypertensive heart. Hypertrophy occurs when there is an increased ventricular wall thickness and stiffness [17].

Likewise, CHDs may be initiated when there are reduced strains in the ventricles; higher end-diastolic stresses and altered cross-fibre stresses can cause vascular aneurysms [18]. For example, verapamil suffusion occurs with decreased pressure in the ventricles with a compact and thinner myocardium [19]. In a recent study, the effects of various disease features on functionality of the heart were modelled [55]. These studies indicated

that LV hypertrophy significantly increased LV pressure, strain, and stroke volume, leading to high mitral regurgitation valve velocities.

In this review, while the cellular-level bulk material properties were only briefly included, complex molecular structures and the material property changes during cellular differentiation deserve dedicated review efforts. For example, cardiomyocytes have a significantly lower value of strength and elastic modulus than hESCs (human embryonic stem cells), showing that the cardiomyocytes lose their strength and elasticity during their specialization, as summarized in Table 5.

5. Conclusions

Material properties of tissues, during development, growth, and disease states, affect how these tissues respond to mechanical forces and their microenvironment. In order to understand and control the vascular structure, the complexity of the cardiovascular system justifies an integrated approach that couples mechano-genetic characteristics with the material properties. Model organisms that possess a biventricular cardiovascular system broadly resemble the human circulation. Due to ethical reasons and experimental challenges, inferences from these model systems are informative for the development of the human heart. Therefore, the present study provides a look-up table of the embryonic material properties across species where human vascular data can be approximately referenced. As such, overall strain and stiffness values tend to increase with age of the developing embryo. It is also observed that the strain values for the LV are consistently higher than for the RV across species. Similarly, ventricular, pressures and size also continue to increase with age. While there is an increase in size, RV continues to grow faster than the LV, maintaining a larger ventricular size and thickness throughout the growth [88]. It is also important to note that the radial strength is generally considerably lower than the longitudinal strength in vascular vessels (Table 5). Genetic signalling also interacts with the mechanical characteristics through the paracrine pathways. Alternatively, studying the genetic patterns can explain changes in the material properties and the body's reaction to these changes. The review also evaluated the consequences of malfunctioning genes and/or abnormal mechanical loading changes and their role in causing CHDs. It is hoped that these inferences concatenate the anatomical, genetic, and mechanical understanding of the heart and further inspire new interdisciplinary studies of complex cardiovascular system.

Chapter 2: Control of mechanosensitive genes during embryonic aortic arch development

1. Introduction

Chick embryos have been excellent model organisms for developmental biology due to the availability of fertilised eggs and the ease in manipulation during embryogenesis. However, genetic manipulation of the embryo and creating mutants challenging since the embryos remain in the oviduct and uterus for the first 24 hours of embryogenesis. This was overcome by In Ovo gene transfer by electroporation making chick embryos a frequently employed and reliable model system. Due to its speed, high specificity and effectiveness, this method proved to be the most efficient method of gene transfer [2]. It allowed the introduction of siRNA into the embryo which knocked down desired genes and the subsequent development of the embryo gave an insight into the functions of the knocked off gene.

Electroporation increases the permeability of the cells by changing the electric field around them allowing the transfer of Genetic material into cells. Application of electroporation ¬in Ovo in chick embryos was unexplored until recently. The popularisation of the technique and the subsequent studies allowed for the optimisation [3] and standardisation of in Ovo electroporation [4]. Nakamura et al. improved the electroporation method to transfect the EN2 (homeobox protein engrailed-2) expression plasmid in the neural tube of the chick embryo [5, 6]. The study of gene expression levels [7], gene knock out [8], knock in [9] and gene function studies [10, 11] were also enabled using in Ovo electroporation. They also induced loss of function with the introduction of siRNA expression vectors by electroporation [12]. In addition, Ueda et al. established a gene delivery system which delivers the genes into spatially restricted domains within the limb bud of chick embryo [13]. The expression of EGFP 24 hours after electroporation has shown the anterior region of the wing field, the posterior region of the wing field and the leg field. These studies were replicated in neural cells [8] while a more recent study [14] indicates that specific tissues can be targeted in any desired region at various stages.

Employing electroporation for knocking out a gene is an interesting way to discover the function of a gene in the developmental stages of an embryo and to see whether a knockout would impact the overall well-being of the embryo. Karakaya et al [1] shows that the expression levels of MMP2 and TGFβ increase as the embryo develops exhibiting

that these genes play an integral part in embryonic aortic arch development unlike the other genes shown in the study (including CDH, ANGTP, TIMP). As abnormalities in MMP2 and TGFβ expression is also known to cause CHDs (congenital heart diseases) these genes were seen as ideal targets to observe whether CHDs could be contained at an embryonic level preventing the need for surgical intervention at later stages. This experiment focuses on knocking out the gene responsible for the production of TGFβ-3 and MMP2 to evaluate the functions of the gene and to see the physiological impact of the knockout.

Before the gene is knocked off, the possibility of visualisation is also to be ensured. This experiment uses green fluorescence protein (GFP) which is proven by many studies to be an effective marker for living embryos [15]. This marker does not harm the embryo and only allows the visualisation. [16] Visualization helps compare the wildtype and the experimental samples.

Using electroporation and GFP as a marker, the role of TGFβ-3 and MMP2 was to be determined. As electroporation has the ability to change the permeability of the cell, it was the chosen gene knockout technique. A potential difference is applied for easy uptake of the siRNA. As soon as the potential difference is removed, the porosity of the cells returns to normal [12]. Despite this, the optimisation of the system was highly essential as a higher charge could cause the embryo to die. Broderick et al worked on optimising the system for dermal tissues [17]. Unfortunately, each organism has a different optimal potential difference and required voltage and this optimization has to be performed individually since a standardised system applicable for all experimental conditions is yet to be established. Hence, in this study, a unique in-house electroporation system was fashioned to perform the experiments [will reference the protocol in the supplementary material].

Once the optimal conditions for the experiment were determined, the process was initiated and observed. This experiment is conducted on chick embryos, but research [18, 19] shows that the same experiments are equally effective and successful for other organisms such as mouse embryos. This shows that the results are reliable and universal.

Electroporation was initially employed to alter the complete organism, but recent research [11, 20] indicates that genes can be electroporated in specific tissues if siRNA is injected at the target site. While loss of function or gain of function studies are used to identify the role of a specific genes in target regions, in Ovo gene electroporation allows

the manipulation of neural and cardiovascular development [21]. This paper considers the possibility of eliminating CHDs by the manipulation of cardiac development using gene knockout at early embryonic stages.

2. Material and Methods:

2.1.Chicken embryo preparation

Fertilized White Leghorn chicken eggs (Gallus gallus domesticus L.) were incubated at 37.5oC and 67% humidity (Kuhl Corp., New Jersey, USA) for 72 hours (~3 days) to obtain embryos that are at the developmental stage HH18. Their stages were determined according to Hamburger Hamilton stages [22].

2.2.In Ovo electroporation

Microinjections were performed using a needle made from glass capillary tubes with a tip opening at ~30 µm in diameter. For the transfection into the aortic arch region of HH18 embryos, a small window was opened on the shell and the vitelline membrane on the embryo was removed to allow siRNA solution to be injected into the middle of the right and the left aortic arches. The glass capillary needles were attached to a holder (Glass Pipette Holder, WPI) mounted on a micromanipulator (Leica). The needle was filled with a mixture of siRNA (TGFβ-3 siRNA-561; 10µl with 20 µM) and 0.4% Trypan Blue (15250-061, Gibco) diluted 4-fold with DEPC (Diethyl pyrocarbonate) water to allow observation of the injection. A pneumatic pressure manipulator was used to inject the siRNA into the target region once the needle was in position.

Three sets of siRNA molecules were obtained from Gene pharma for TGFβ-3 gene (Shanghai, China). These were siRNA-561, 846 and 983 with Cy5 tag and one set was obtained for MMP2 gene.

A pair of electrodes were set on a micromanipulator and placed on the vitelline membrane at 4 mm apart. A small volume of Chick Ringer solution (135mM NaCl, 4mM KCI, 10mM Trizma-HCI, 10mM Trizma-base, 11mM Dextrose, 2mM CaCI2) was dropped between the electrodes. A custom code was developed to apply charge at uniform intervals for 40 cycles. Then the square pulses (13.5V, 50 ms/each) were charged by the power supplier. A few drops of the Chick Ringer solution were added again to prevent damage from occurring at the point where the electrodes were directly attached. After electroporation, the window on the operated eggs was sealed with Parafilm, and the eggs were incubated until HH24 (~1 day).

2.3.Imaging

Microscopic analysis and visualization of electroporated embryos were performed using a confocal microscope (AZ100, Nikon). After incubation, HH24 reaching embryos were extracted from the egg and transferred to the Krebs solution for imaging. Images of the Cy5-expressed tissues were obtained using a laser of wavelength 642 and a spectral detector. Afterwards, aortic arch tissues were extracted from Cy5 positive embryos under the stereo microscope (Stemi 305, ZEISS). The right and the left aortic arch tissues were separately obtained using micro-tweezer and scissor as seen in figure C2 1. Then they were transferred to the RNAlater solution (Sigma Aldrich).

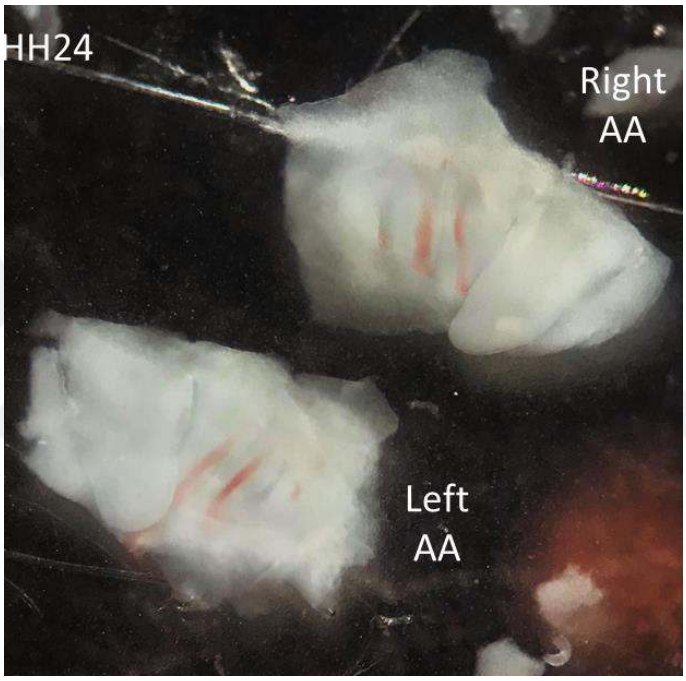

Figure C2 1: At HH24, after confocal imaging, the cy tagged siRNA injected aortic arches are excised for PCR. Since the expression levels in the aortic arch region are asymmetric [1], the left and right are individually evaluated after excision.

2.4.Simulation

A finite element model was created to predict the effect of the knockout of MMP2 and TGFb3. Springs were used to determine the cross-sectional view of the aortic arch region to evaluate the thickness and diameter of the embryo during development. Collagen and elastin which are downstream genes for MMP2 and TGFb3 respectively were represented using blue and red colours respectively for feasible distinction. Collagen fibres were simulated as springs aligned in radial and circumferential directions while the elastin springs were attached to the circumferential collagen springs. This idealised model

accounted for the pressure and wall shear stress which were calculated experimentally and entered. The initial condition for both the models were kept constant to evaluate the differences. Experimentally obtained results pertaining to thickness and diameter of the AA were then compared to the simulations.

2.5.RNA isolation and reverse transcription-quantitative PCR (RT-qPCR)

As described previously [1], total RNA from the right and left aortic arch of sham and siRNA applied embryos was isolated using GeneJET RNA purification kit (Thermo Scientific). The purity and concentration of the RNA samples were quantified with Nanodrop 2000c spectrophotometer (Thermo Scientific). RT-qPCR was performed using Luminaris Color HiGreen qPCR Master Mix (Thermo Scientific) to measure the expression levels of TGFβ-3, TGFβ-2, FBN-1, COL1, COL3 and ELN. Each sample was loaded on the RT-qPCR plate as triplicates and at least three biological replicates were used for each gene. Forward and reverse primer sequences were designed in Beacon Designer Software (Supplementary Table1). The conditions for the reaction were initial denaturation at 95^{o}C for 10 min followed by a three-step cycle of denaturation at 95oC for 15s, annealing at 60^{o}C for 30s and extension at 72^{o}C for 30s, repeated 40 times. Only ELN had a different annealing temperature of 62^{o}C. Glyceraldehyde 3-phosphate dehydrogenase (GAPDH) was chosen as a control gene to normalize the relative expression level of the genes using 2^ (-〖ΔΔC〗_T) method [23]. Besides, fold changes were represented based on expressions of sham sample as a negative control for all genes.

2.6.Protein detection using western blotting

Though confocal imaging can be used to ensure that the gene was knocked out, western blotting was used as a second validation method. Protein was isolated from control, sham and electroporated aortic arch tissues and homogenised using RIPA buffer and protein inhibitor complex (PIC). The thus obtained lysate was loaded with 5X Laemmli buffer in 12% SDS-PAGE gel. A 10X running buffer was used during electrophoresis. The proteins were then transferred to PVDF membranes using wet transfer. Blots were probed with anti-MMP2 and anti-GAPDH followed by an HRP conjugated anti-mouse secondary antibody. TMB substrates were applied, and the membrane was imaged using a CCD camera (western blot imaging system).

2.7.Physiological Analysis

After electroporation at HH16, samples were incubated till HH24. OCT was performed in Ovo for the aortic arches of these samples using Thorlabs Spectral Domain OCT System. The equivalent diameter was calculated using ImageJ software and the mid-point diameter was obtained. OCT images were also obtained for non-electroporated samples at HH24 and were used as controls. The diameters were compared with literature and the results were recorded.

2.8.Statistical Analysis

GraphPad Prism version 8.0.0 was used to conduct statistical analysis. After that two-way analysis of variance (ANOVA) and post-hoc Tukey HSD were performed to determine the____ and the significance level was adjusted to $p<0.05$. All data were presented as the mean ± standard deviation.

3. Results:

The results are divided into 3 parts: simulated predictions, confocal imaging, evaluation of gene expression levels and verification. Using the finite element model, simulations were generated for MMP2 and TGFb3 Knockout samples. The simulations in figure C2 2 depicts the simulated cross-section of the AA at HH18 and HH24 respectively. The graphical representation of the level of collagen, elastin and the physiological impact of these changes allows an easy comparison between the simulated samples. Pressure and wall shear stresses are selected according to experimental values. An increase in diameter can only be observed for MMP2 knockout samples.

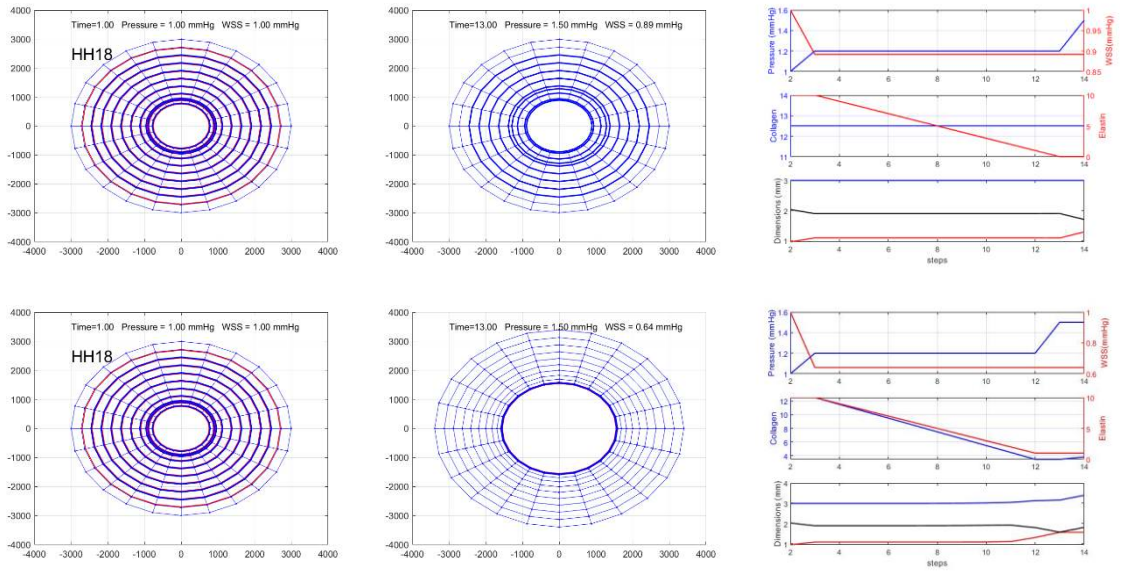

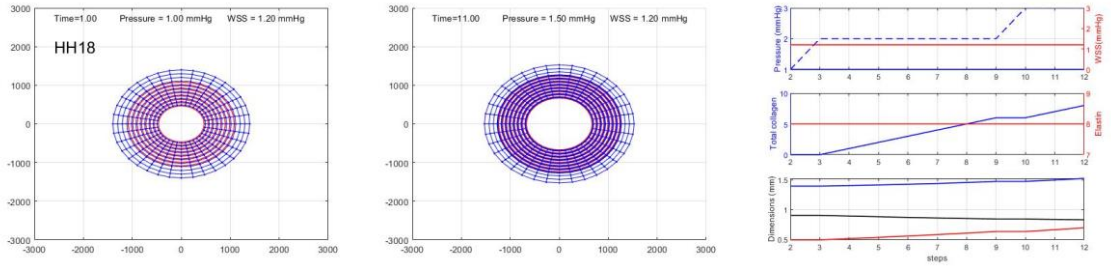

Figure C2 2: TOP: Simulations for TGFb3 knockout showing a decrease in elastin levels but no significant increase in thickness and diameter. MIDDLE: Simulations showing MMP2 knockouts exhibit an increase in thickness and diameter corresponding to the decrease in collagen levels. BOTTOM: The control sample showing constant and consistent growth in thickness and diameter.

The simulated results need to be verified experimentally. After electroporation and microinjection of the cy-5 tagged siRNA into the AA, the target region is observed under a confocal microscope to evaluate whether the siRNA was incorporated into the target region (aortic arch region). The confocal images pick signals from the cy5 dye, and the AA region is illuminated as shown in figure C2 3.

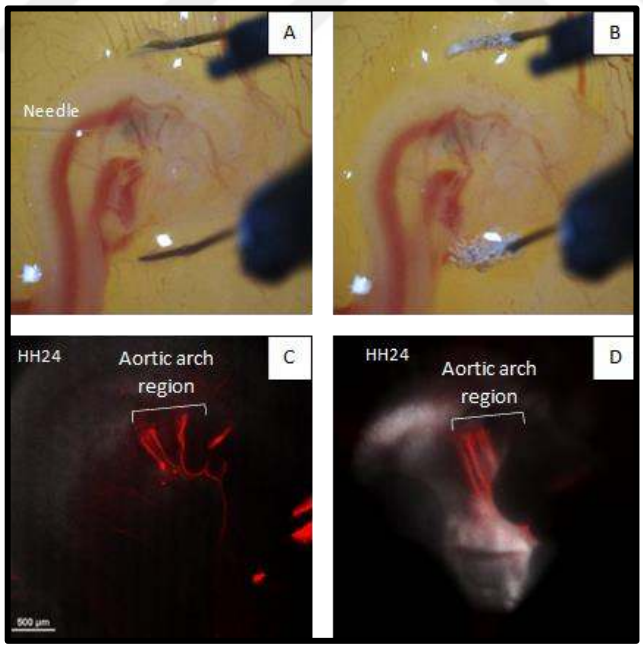

Figure C2 3: A. The experimental setup used to inject chick embryos at HH16 (aortic arch region) with cy5 tagged siRNA. The first and second protective layers around the embryo are removed prior to injection for easier access to the aortic arch region. B. The two electrodes are placed around the target region and a potential difference of 13.5 Volts is applied causing the bubbles to appear as shown on the right. C, D. Confocal imaging at

HH24 (aortic arch, aa) shows the fluorescent siRNA A stage HH16 chick embryo imaged under a stereomicroscope is also provided. B. Preliminary hours after injection and electroporation.

The samples showing positive signals in confocal imaging are selected for the evaluation of gene expression. The PCR results are evaluated, and the relative gene expression for each gene is measured. As shown by Karakaya et al, [1] the gene expression levels in the left and right AA are unique thus the expression levels are compared with control and sham samples for both left and right AA. A comparison of the different types of TGFβ-3 siRNA is also performed to show the most effective siRNA for TGFβ-3 knockout.

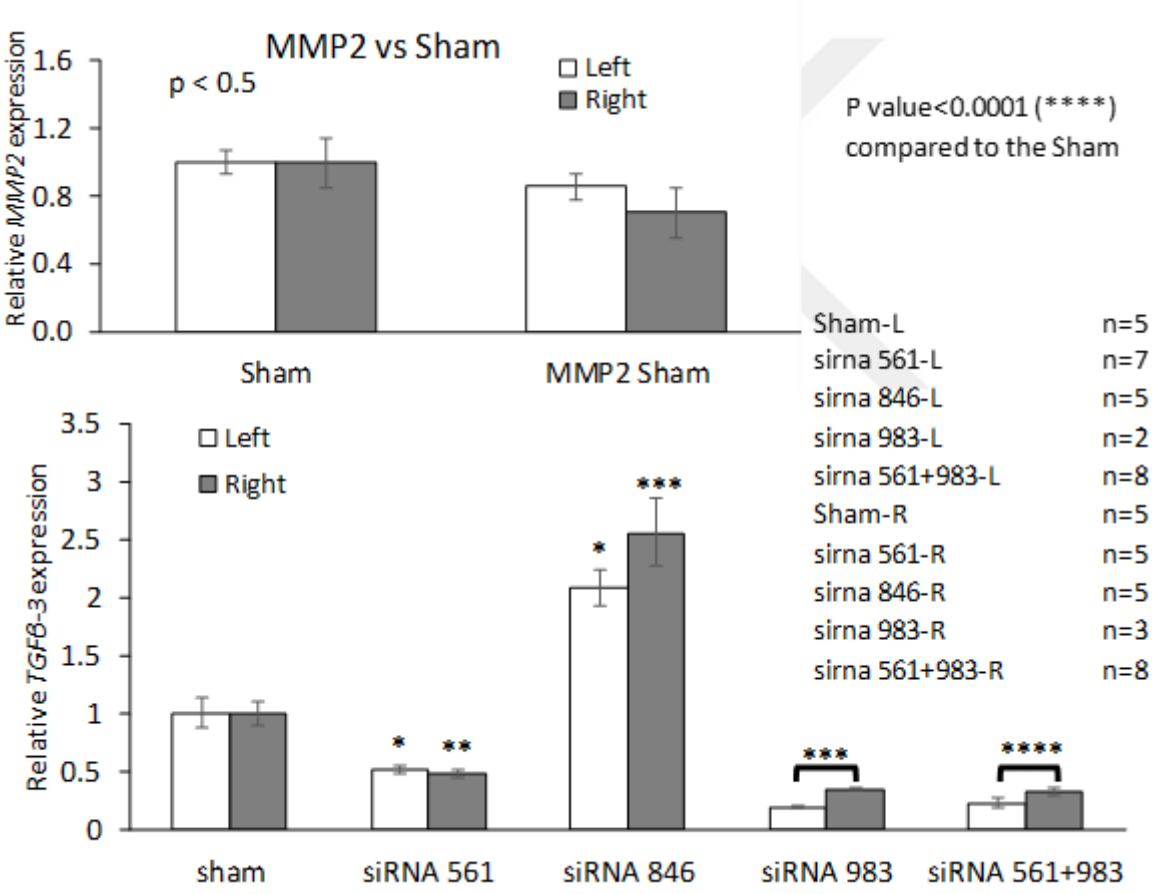

Figure C2 4: RT-qPCR results of MMP2 and TGFβ-3 expression levels using GAPDH as housekeeping gene. Sham samples are used as control to compare the expression levels before and after electroporation and specific gene knockout. P values are calculated for each experiment and represented as shown. The number of samples for each experiment are represented by n.

Figure C2 4 shows the relative expression levels of TGFβ-3 and MMP2. It is observed that in most cases, the expression levels in the left AA are lower than the right AA for TGFβ-3 while for MMP2, the expression levels are higher in the left AA. It is also inferred that the most effective siRNA for TGFβ-3 knockout is a cocktail of siRNA 561 and siRNA 983. When using other siRNA, the results are similar but not as significant except for siRNA 846. The p-values for these experiments were all below 0.5.

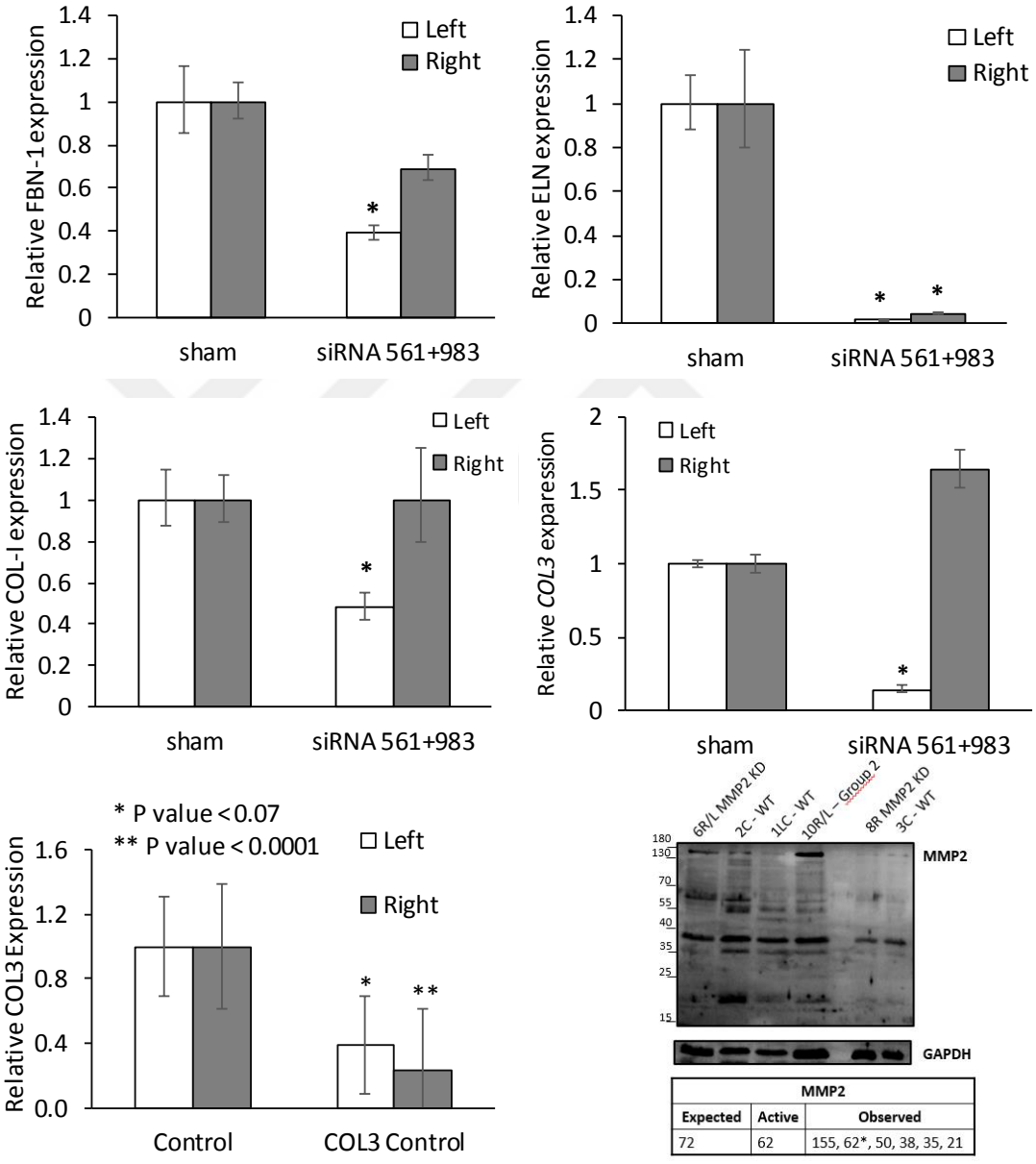

Figure C2 5: A. RT-qPCR results of downstream gene expression levels using GAPDH as housekeeping gene. FBN-1, ELN, COL1 and COL3 are downstream genes for TGFβ-3 knockout B. A. RT-qPCR results of MMP2 downstream gene expression (COL3) levels using GAPDH as housekeeping gene. Sham samples are used as control

to compare the expression levels before and after gene knockout. P values are calculated for each experiment and represented as shown. The number of samples for each experiment are represented by n. Western blotting results are shown in the bottom right figure, we see prominent bands at 155, 62, 50, 35, 38 and 21 kDa.

Since genes form a complex network and act codependently, it is important to observe the impact of the knockout on the downstream genes. For TGFβ-3, as it is crucial in growth of organisms and in angiogenesis, downstream genes such as FBN-1, ELN, COL-I and COL-III were studied for their relative expression. As shown in figure C2 5, gene expression levels of most genes reduce, and the knockout affects the left AA more. However, COL-I expression in the right AA remains the same and COL-III expression in the right AA increases.

A similar analysis was conducted for MMP2 knockout. The gene expression levels for COL-III were studied and it was found that knockout of MMP2 is more effective in reducing gene expression of COL-III than the knockout of TGFβ-3

Following this, verification tests were performed in two parts. Firstly, the specificity of gene knockout was determined by western blotting analysis. For this, primer specificity was established by obtaining the sequences of all similar gene. BLAST was used to align the sequences of MMP's with the sequences of the forward and reverse primers. It was seen that there was no overlapping sequence between the primers and other MMP's. To further verify the results, the forward and reverse primers were run through agar gel, and it was observed that the gel showed one clear and distinct line showing that the primers were specific. Then, gene specific antigens were used to analyse the knockout samples. The left and the right arches were simultaneously evaluated for the presence of MMP2. Wild type samples and knockout samples were compared in the same gel. MMP2 is usually observed at 72 kDa but has an active form at 62 kDa hence, thick bands were expected at either 72 kDa or at 62 kDa for the control sample and an absence or thin bands were expected at the same location for the knockout samples. However, the western blotting results showed bands at 155, 62, 50, 35, 38 and 21 kDa for both, the control and the knockout samples. These results are inconsistent with the expected outcome. Meanwhile, the inhouse gene, GAPDH, showed bands of desired thickness at the expected location proving that, despite the inconsistent results, the experiment was successful.

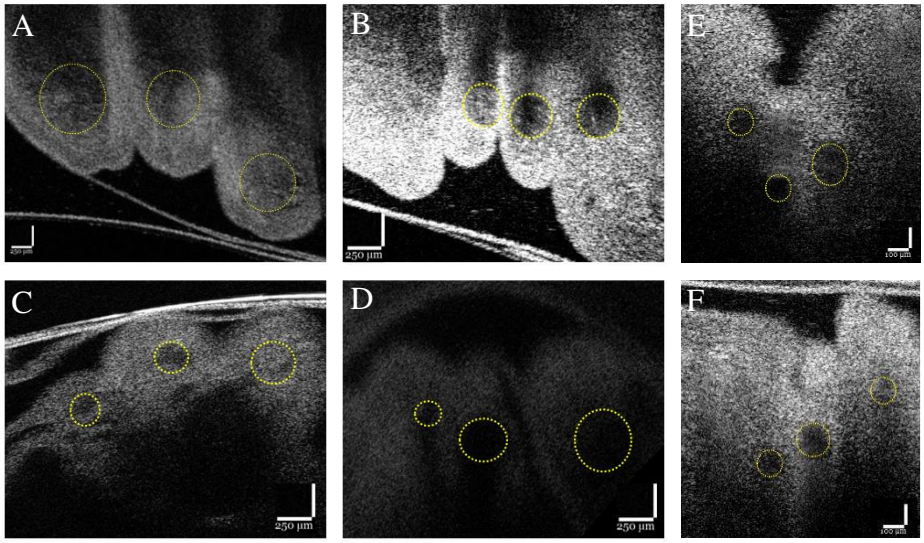

Figure C2 6: The OCT images indicating the diameters of the IIIrd, IVth and VIth aortic arches of the electroporated samples at HH24 for MMP2 (A, B, C and D) and the TGFb-3 (E and F) knocked out samples. These images were taken in Ovo thus have some distortions due to the embryonic heartbeat. These samples were compared, and the values were recorded in table 1.

The second verification was physiological. The diameter of the targeted aortic arch region was obtained using OCT imaging as seen in the Figure C2 6. The I, II and V aortic arches are no longer visible at HH24, hence in this paper, the diameters of the III, IV and VI arches are obtained. The calculated diameters were compared to the expected diameters at HH24 and compared. Table 1 shows the experimentally obtained data. It was observed that for the MMP2 knockout samples, the diameter of the arches significantly increased upon electroporation, and in some cased, nearly doubled. The change in diameter is expected as MMP2 controls the collagen levels and the knockout of MMP2 would cause structural changes in the target region. Similarly, TGFb3 controls elastin levels and hence the impact of the knockout is observed for elastin. The thickness and the diameter both show a small increase in value despite not being as significant as the increase in MMP2 knockout samples. Elastin does not directly impact the thickness and the diameter and hence these results align with the expected results. This novel finding has the potential to change the course of in Ovo and in vitro genetic modifications to prevent CHD's.

Table C2 1: Mid-point diameter of the aortic arches at HH24 after MMP2 and TGFb3 knockout in the AA region

AA	Side	MMP2 KO (mm)			TGFb3 KO (mm)			Normal Diameter (mm) [24]
		Diameter	Thickness	n	Diameter	Thickness	n	
III	L	0.248 ± 0.039	0.247	6	0.170 ± 0.023	0.174	7	0.112 ± 0.015
	R	0.289 ± 0.076	0.283	8	0.155 ± 0.019	0.158	9	0.123 ± 0.016
IV	L	0.301 ± 0.043	0.249	4	0.159 ± 0.020	0.153	4	0.118 ± 0.019
	R	0.245 ± 0.063	0.203	7	0.165 ± 0.032	0.099	8	0.140 ± 0.024
VI	L	0.290 ± 0.097	0.265	4	0.174 ± 0.030	0.100	8	0.113 ± 0.019
	R	0.302 ± 0.041	0.272	5	0.134 ± 0.035	0.139	9	0.138 ± 0.024

The same analysis was performed for TGFβ-3 knocked out sample and similar to MMP2 Knockouts, an increase in diameter was observed as shown in table 1. However, as seen in C2 6, the increase in diameter in TGFβ-3 knockout sample is much lesser than in MMP2 knockout sample.

Figure C2 6 shows that for the aortic arches II, III and V in MMP2 knockouts the diameter is higher while TGFb3 knockout has lower diameter. When compared with normal data, TGFb3 diameter does not significantly change. We also observe that the thickness of the TGFb3 knockout sample does not exhibit a drastic increase in the value while MMP2 knockout samples do.

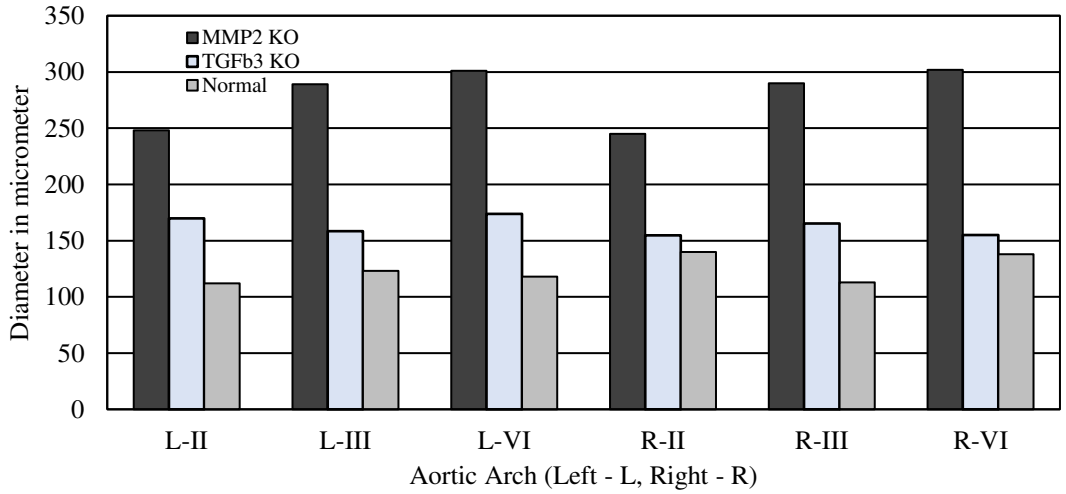

Figure C2 7: Graphical representation of the diameters of the MMP2 and TGFb3 knockout samples compared with the wild-type control samples. A drastic increase in the diameter is observed for MMP2 knockout

4. Discussion:

Microinjection and electroporation are the selected mode of gene delivery in this experiment and have been proven to be highly effective. RT -q PCR was chosen as the primary validation method for observing target gene expression levels pre and post knockout as it is a reliable, accurate and highly sensitive method. Housekeeping genes have low genetic diversity and are conserved in their functions due to which they are chosen as reference genes. GAPDH has been found to be one of the most highly stable and conserved genes [25] and hence was used in our experiment as the housekeeping gene. The expression levels of amplified samples are calculated by finding the Ct values of the genes. RT-qPCR shows the expression levels of the genes but as the genes are knocked out, but gene specificity is analysed using western blotting. For our experiment, since the knocked-out genes are unique, the purpose of western blotting is mainly for a secondary validation.

The graphs in figure 3 indicate that prior to knockout, gene expression levels for the target gene are significantly higher proving that the knockout has been successful. Figure 4 also displays the results for downstream gene expression levels showing that the MMP2 and TGFβ-3 knockout successfully impacts the proteins downstream and hence will cause desirable changes in the physiology of the cardiac system during development. For a thorough analysis, figure C2 5 also reports the western blotting results of protein expression levels of target protein MMP2 and the results are inconsistent with the RT-qPCR results. GAPDH bands were observed at the accurate locations proving that the experiment was successful.

A thick band was expected to be seen at 72 or 62 kDa for the control since MMP2 is usually visible at 72 kDa but has an active form for humans and chicks at 62 kDa. A thin band or no band at the same locations for the knockout samples. However, the observed results showed a thick band at 155, 62, 50, 38, 35 and at 21 kDa for both the control and the knockout samples. As the aortic arch region is small in the developing embryo, it is challenging to isolate a sufficient amount to perform western blotting. To ensure that the tissue content was desirable for the experiments, tissues from multiple electroporated chick embryos were collected and used for a single western blot. However, due to the small size of the tissue, isolation of solely the target region was not feasible. Excess tissue has the potential to tamper the results and hence the results showed bands at unexpected locations. RT-qPCR requires a small amount of tissue sample and hence has a much lower

possibility of having non-target tissue in the sample. Thus, embryonic aortic arches pose a unique hurdle due to their small size and difficulty in isolation which can be overcome by RT-qPCR but renders western blotting as an ineffective tool to verify the results.

Thus, these RT-qPCR results are reliable and replicable for a given gene. It also has the capacity to predict physiological cardiac changes as the embryo develops preventing predictable CHD's.

Certain genes play a crucial role in the control of embryonic development. The selected genes for knockout, TGFβ-3 and MMP2 are known to play a role in angiogenesis. MMP's are responsible for metallopeptidase activity (Catalysis of the hydrolysis of internal, alpha-peptide bonds in a polypeptide chain by a mechanism in which water acts as a nucleophile, one or two metal ions hold the water molecule in place and charged amino acid side chains are ligands for the metal ions.). MMP2 specifically enables the gelatin type I and COL cleavage (Cleavage of gelatin type I and collagen types IV, V, VII, X. Cleaves the collagen-like sequence Pro-Gln-Gly-|-Ile-Ala-Gly-Gln.). Thus, MMP2 controls extracellular matrix (ECM) organisation, tissue remodelling, cardiac cushion cell migration and blood vessel maturation. It also positively regulates vascular associated smooth muscle cell proliferation and negatively regulates cartilage development which in turn mediates neural crest and cardiac development [26]. Initially, MMP2 is expressed during the formation of heart tube in cardiogenic splanchnic mesoderm and at sites of active pharyngeal arch showing that MMP2 plays a role in early cardio genesis. Literature shows that MMP2 (MMP2rs2285053 TC genotype) increases susceptibility to Thoracic Aortic Aneurysms [27]. It was proven that angiotensin II-induced vascular injury is prevented by MMP2 knockout [28].

The downstream genes for MMP2 are COL's, when studying the expression levels of COL III, it was seen that the expression levels of downstream genes are also reduced. COL's are a structural component which control tensile strength and are ECM constituents. They play a role in branching blood vessel morphogenesis, blood vessel development and ECM organisation. MMP2 has an expression score of 85.85. Targeted MMP2 knockdown can thus control cardiogenesis and the stiffness of the vessels during angiogenesis.

A recent study shows that TGFβ is essential for cardiac development [29] and defects in its expression can cause various abnormalities [30]. Hence controlling TGFβ expression levels would allow targeted manipulation of cardiogenesis and prevent

abnormalities such as arrhythmogenic right ventricular dysplasia/cardiomyopathy (ARVD1) and Loeys-Dietz syndrome-5 (LDS5)/Rienhoff syndrome which are associated with cardiomyopathy, cardiac arrhythmia, cardiac fibrosis, cleft palate, aortic aneurysms, and valvular heart disease [29]. Defects in TGFβ also affect pulmonary development, cause defects in cleft palate [31], bicuspid aortic valve disease [32] and coronary artery disease [33]. Abnormal TGFβ signalling causes Marfan and Loeys-Dietz syndromes while syndromic aortic aneurysms and dissections are caused by mutant TGFβ ligands [34].

While the findings in literature point to possible changes in the physiology of gene knockout target region, our experimental results of MMP2 knockout obtained from OCT prove that there are significant and evident changes in the aortic arch region. The results show that the diameter increases substantially in all aortic arches. It is important to note that the development of the embryo is not affected as the changes in diameter do not prevent the disappearance of the IInd arch and the formation of the VIth arch. The IIIrd aortic arch's diameter increases over two folds in both the right and the left arches while maintaining that the right aortic arch has a higher diameter than the left as demonstrated to be the case by Karakaya et al [1]. The diameters of the aortic arches were compared to the data presented by Wang et al. [24] and it was seen that the IVth left aortic arches have a higher increase than the right arches in diameter thus causing the diameter of the left arch to be greater than the right. For the VIth arch, similar to the IIIrd arch, despite a higher increase in diameter for the left arch, the right arch maintains a higher diameter at HH24. These findings open new opportunities in enabling early elimination of CHD's at an embryonic level. Patients with genetic cardiac diseases can resort to eliminate these diseases at a molecular level thus preventing unwarranted surgeries at later stages.

5. Conclusion:

Literature shows that MMP2 and TGFβ play crucial roles in essential cardiogenesis and angiogenesis. This study presents a breakthrough finding that these genes can be manipulated at an in Ovo embryonic level using electroporation and microinjection for chick embryos (Gallus Gallus Domesticus) as a model organism. The successful knockout of MMP2 and TGFβ-3 opens new doors for therapies at an embryonic stage for patients with CHD's and low mortality rate. Studies also shows that since TGFβ play a crucial role in cardiogenesis, controlling its expression levels can also facilitate repair and rehabilitation in cardiovascular diseases in adults [35].

Following this research, chicks induced with CHD's can be genetically modified at the embryonic level and the embryo can be allowed to develop into a chick. The heart can then be surgically and genetically evaluated for evidence of the absence of CHD's.

BIBLIOGRAPHY

CHAPTER 1 REFERENCES

1. Nye, K.S.; Esplin, M.S.; Monson, K.L. Umbilical cord artery mechanical properties at various gestational ages. Am. J. Perinatol. 2015, 32, 263–270.
2. Li, P.; Liu, A.; Shi, L.; Yin, X.; Rugonyi, S.; Wang, R.K. Assessment of strain and strain rate in embryonic chick heart in vivo using tissue Doppler optical coherence tomography. Phys Med Biol. 2011, 56, 7081–7092.
3. Karimi, A.; Navidbakhsh, M.; Rezaee, T.; Hassani, K. Measurement of the circumferential mechanical properties of the umbilical vein: Experimental and numerical analyses. Comput Methods Biomech Biomed Engin. 2015, 18, 1418–1426.
4. Lucitti, J.L.; Tobita, K.; Keller, B.B. Arterial hemodynamics and mechanical properties after circulatory intervention in the chick embryo. J. Exp. Biol. 2005, 208, 1877–1885.
5. Gjorevski, N.; Nelson, C.M. The mechanics of development: Models and methods for tissue morphogenesis. Birth Defects Res. C Embryo Today 2010, 90, 193–202.
6. Forouhar, A.S.; Liebling, M.; Hickerson, A.; Nasiraei-Moghaddam, A.; Tsai, H.J.; Hove, J.R.; Fraser, S.E.; Dickinson, M.E.; Gharib, M. The embryonic vertebrate heart tube is a dynamic suction pump. Science 2006, 312, 751–753.
7. Yang, M.; Taber, L.A.; Clark, E.B. A nonliner poroelastic model for the trabecular embryonic heart. J. Biomech. Eng. 1994, 116, 213–223.
8. Yao, J.; Varner, V.D.; Brilli, L.L.; Young, J.M.; Taber, L.A.; Perucchio, R. Viscoelastic material properties of the myocardium and cardiac jelly in the looping chick heart. J. Biomech. Eng. 2012, 134, 024502.
9. Taber, L.A.; Keller, B.B.; Clark, E.B. Cardiac mechanics in the stage-16 chick embryo. J. Biomech. Eng. 1992, 114, 427–434
10. Tobita, K.; Keller, B.B. Right and left ventricular wall deformation patterns in normal and left heart hypoplasia chick embryos. Am. J. Physiol.-Heart Circ. Physiol. 2000, 279, H959–H969.

11. Tobita, K.; Garrison, J.B.; Liu, L.J.; Tinney, J.P.; Keller, B.B. Three-dimensional myofiber architecture of the embryonic left ventricle during normal development and altered mechanical loads. Anat. Rec. A Discov. Mol. Cell. Evol. Biol. 2005, 283, 193–201.
12. Donmazov, S.; Piskin, S.; Pekkan, K. Noninvasive in vivo determination of residual strains and stresses. J. Biomech. Eng. 2015, 137, 061011.
13. Kasyanov, V.; Moreno-Rodriguez, R.A.; Kalejs, M.; Ozolanta, I.; Stradins, P.; Wen, X.; Yao, H.; Mironov, V. Age-related analysis of structural, biochemical and mechanical properties of the porcine mitral heart valve leaflets. Connect. Tissue Res. 2013, 54, 394–402.
14. Zhuan, X.; Luo, X. Residual Stress Estimates from Multi-cut Opening Angles of the Left Ventricle. Cardiovasc. Eng. Technol. 2020, 11, 381–393.
15. Nabati, M.; Namazi, S.S.; Yazdani, J.; Sharif Nia, H. Relation Between Aortic Stiffness Index and Distensibility with Age in Hypertensive Patients. Int. J. Gen. Med. 2020, 13, 297–303.
16. Ishizu, T.; Seo, Y.; Kameda, Y.; Kawamura, R.; Kimura, T.; Shimojo, N.; Xu, D.; Murakoshi, N.; Aonuma, K. Left ventricular strain and transmural distribution of structural remodeling in hypertensive heart disease. Hypertension 2014, 63, 500–506.
17. Vejdani-Jahromi, M.; Nagle, M.; Trahey, G.E.; Wolf, P.D. Ultrasound shear wave elasticity imaging quantifies coronary perfusion pressure effect on cardiac compliance. IEEE Trans. Med. Imaging. 2015, 34, 465–473.
18. Walker, J.C.; Ratcliffe, M.B.; Zhang, P.; Wallace, A.W.; Hsu, E.W.; Saloner, D.A.; Guccione, J.M. Magnetic resonance imaging-based finite element stress analysis after linear repair of left ventricular aneurysm. J. Thorac. Cardiovasc. Surg. 2008, 135, 1094–1102.
19. Buffinton, C.M.; Faas, D.; Sedmera, D. Stress and strain adaptation in load-dependent remodeling of the embryonic left ventricle. Biomech. Model. Mechanobiol. 2013, 12, 1037–1051.
20. Stekelenburg-de Vos, S.; Steendijk, P.; Ursem, N.T.; Wladimiroff, J.W.; Poelmann, R.E. Systolic and diastolic ventricular function in the normal and extra-embryonic venous clipped chicken embryo of stage 24: A pressure-volume loop assessment. Ultrasound Obstet. Gynecol. 2007, 30, 325–331.

21. Groenendijk, B.C.; Hierck, B.P.; Gittenberger-De Groot, A.C.; Poelmann, R.E. Development-related changes in the expression of shear stress responsive genes KLF-2, ET-1, and NOS-3 in the developing cardiovascular system of chicken embryos. Dev. Dyn. 2004, 230, 57–68.
22. Groenendijk, B.C.; Hierck, B.P.; Vrolijk, J.; Baiker, M.; Pourquie, M.J.; Gittenberger-de Groot, A.C.; Poelmann, R.E. Changes in shear stress-related gene expression after experimentally altered venous return in the chicken embryo. Circ. Res. 2005, 96, 1291–1298.
23. Taber, L.A.; Voronov, D.A.; Ramasubramanian, A. The role of mechanical forces in the torsional component of cardiac looping. Ann. N. Y. Acad. Sci. 2010, 1188, 103–110.
24. Wessels, A.; Markwald, R. Cardiac morphogenesis and dysmorphogenesis. I. Normal development. Methods Mol. Biol. 2000, 136, 239–259.
25. Davidson, L.A. Mechanical design in embryos: Mechanical signalling, robustness and developmental defects. Philos Trans. R. Soc. Lond. B Biol. Sci. 2017, 372, 20150516
26. Schulze-Bauer, C.A.J.; Morth, C.; Holzapfel, G.A. Passive Biaxial Mechanical Response of Aged Human Iliac Arteries. J. Biomech. Eng. 2003, 125, 395–406.
27. Ferrara, A.; Morganti, S.; Totaro, P.; Mazzola, A.; Auricchio, F. Human dilated ascending aorta: Mechanical characterization via uniaxial tensile tests. J. Mech. Behav. Biomed. Mater. 2016, 53, 257–271.
28. Ross, C.; Laurence, D.; Wu, Y.; Lee, C.-H. Biaxial Mechanical Characterizations of Atrioventricular Heart Valves. J. Vis. Exp. 2019, 9, e59170.
29. Murdock, K.; Martin, C.; Sun, W. Characterization of mechanical properties of pericardium tissue using planar biaxial tension and flexural deformation. J. Mech. Behav. Biomed. Mater. 2018, 77, 148–156.
30. Miller, C.E.; Wong, C.L.; Sedmera, D. Pressure overload alters stress-strain properties of the developing chick heart. Am. J. Physiol.-Heart Circ. Physiol. 2003, 285, H1849–H1856.
31. Li, Y.; Zheng, J.; Bird, I.M.; Magness, R.R. Mechanisms of shear stress-induced endothelial nitric-oxide synthase phosphorylation and expression in ovine fetoplacental artery endothelial cells. Biol. Reprod. 2004, 70, 785–796.

32. Filas, B.A.; Xu, G.; Taber, L.A. Probing regional mechanical properties of embryonic tissue using microindentation and optical coherence tomography. Methods Mol. Biol. 2015, 1189, 3–16.
33. Smoljkic, M.; Vander Sloten, J.; Segers, P.; Famaey, N. Non-invasive, energy-based assessment of patient-specific material properties of arterial tissue. Biomech Model. Mechanobiol. 2015, 14, 1045–1056.
34. Joshi, S.D.; Kim, H.Y.; Davidson, L.A. Microscopy tools for quantifying developmental dynamics in Xenopus embryos. Methods Mol. Biol. 2012, 917, 477–493.
35. Gendernalik, A.; Zebhi, B.; Ahuja, N.; Garrity, D.; Bark, D.Jr. In Vivo Pressurization of the Zebrafish Embryonic Heart as a Tool to Characterize Tissue Properties During Development. Ann. Biomed. Eng. 2021, 49, 834–845.
36. Teal, S.I.; Moore, G.W.; Hutchins, G.M. Development of aortic and mitral valve continuity in the human embryonic heart. Am. J. Anat. 1986, 176, 447–460.
37. Tan, Y.; Kong, C.W.; Chen, S.; Cheng, S.H.; Li, R.A.; Sun, D. Probing the mechanobiological properties of human embryonic stem cells in cardiac differentiation by optical tweezers. J. Biomech. 2012, 45, 123–128.
38. Clavero Adell, M.; Ayerza Casas, A.; Jimenez Montanes, L.; Palanca Arias, D.; Lopez Ramon, M.; Alcala Nalvaiz, J.T.; Samper Villagrasa, P. Evolution of strain and strain rate values throughout gestation in healthy fetuses. Int. J. Cardiovasc. Imaging. 2020, 36, 59–66.
39. Taketazu, M.; Sugimoto, M.; Saiki, H.; Ishido, H.; Masutani, S.; Senzaki, H. Developmental Changes in Aortic Mechanical Properties in Normal Fetuses and Fetuses with Cardiovascular Disease. Pediatr. Neonatol. 2017, 58, 245–250.
40. Smoljkic, M.; Verbrugghe, P.; Larsson, M.; Widman, E.; Fehervary, H.; D'Hooge, J.; Vander Sloten, J.; Famaey, N. Comparison of in vivo vs. ex situ obtained material properties of sheep common carotid artery. Med. Eng. Phys. 2018, 55, 16–24.
41. Van der Heiden, K.; Groenendijk, B.C.; Hierck, B.P.; Hogers, B.; Koerten, H.K.; Mommaas, A.M.; Gittenberger-de Groot, A.C.; Poelmann, R.E. Monocilia on chicken embryonic endocardium in low shear stress areas. Dev. Dyn. 2006, 235, 19–28.

42. Rodriguez, M.; Juran, C.; McClendon, M.; Eyadiel, C.; McFetridge, P.S. Development of a mechanically tuneable 3D scaffold for vascular reconstruction. J. Biomed. Mater. Res. A 2012, 100, 3480–3489.
43. Lin, I.E.; Taber, L.A. Mechanical effects of looping in the embryonic chick heart. J. Biomech. 1994, 27, 311–321.
44. Disney, C.M.; Lee, P.D.; Hoyland, J.A.; Sherratt, M.J.; Bay, B.K. A review of techniques for visualising soft tissue microstructure deformation and quantifying strain Ex Vivo. J. Microsc. 2018, 272, 165–179.
45. Lashkarinia, S.S.; Coban, G.; Ermek, E.; Celik, M.; Pekkan, K. Spatiotemporal remodeling of embryonic aortic arch: Stress distribution, microstructure, and vascular growth in silico. Biomech. Model. Mechanobiol. 2020, 19, 1897–1915.
46. Xu, G.; Kemp, P.S.; Hwu, J.A.; Beagley, A.M.; Bayly, P.V.; Taber, L.A. Opening angles and material properties of the early embryonic chick brain. J. Biomech. Eng. 2010, 132, 011005.
47. Trier, S.M.; Davidson, L.A. Quantitative microscopy and imaging tools for the mechanical analysis of morphogenesis. Curr. Opin. Genet. Dev. 2011, 21, 664–670.
48. Ogden, R.W. Nonlinear Elasticity, Anisotropy, Material Stability and Residual Stresses in Soft Tissue. In Biomechanics of Soft Tissue in Cardiovascular Systems; Holzapfel, G.A., Ogden, R.W., Eds.; Springer: Vienna, Austria, 2003; pp. 65–108.
49. Buskohl, P.R.; Gould, R.A.; Butcher, J.T. Quantification of embryonic atrioventricular valve biomechanics during morphogenesis. J. Biomech. 2012, 45, 895–902.
50. Zamir, E.A.; Taber, L.A. Material Properties and Residual Stress in the Stage 12 Chick Heart During Cardiac Looping. J. Biomech. Eng. 2005, 126, 823–830.
51. Ogden, R.W.; Hill, R. Large deformation isotropic elasticity—On the correlation of theory and experiment for incompressible rubberlike solids. Proc. R. Soc. Lond. A Math. Phys. Sci. 1972, 326, 565–584.
52. von Dassow, M.; Strother, J.A.; Davidson, L.A. Surprisingly Simple Mechanical Behavior of a Complex Embryonic Tissue. PloS one. 2011, 5, e15359.

53. Fung, Y.C. Biomechanics: Mechanical Properties of Living Tissues; Springer: New York, NY, USA, 1981.
54. Chuong, C.J.; Fung, Y.C. Three-Dimensional Stress Distribution in Arteries. J. Biomech. Eng. 1983, 105, 268–274.
55. Ong, C.W.; Ren, M.; Wiputra, H.; Mojumder, J.; Chan, W.X.; Tulzer, A.; Tulzer, G.; Buist, M.L.; Mattar, C.N.; Lee, L.C.; et al. Biomechanics of Human Fetal Hearts with Critical Aortic Stenosis. Ann. Biomed. Eng. 2021, 49, 1364–1379.
56. Sáez, P.; Peña, E.; Martínez, M.A.; Kuhl, E. Computational modeling of hypertensive growth in the human carotid artery. Comput. Mech. 2014, 53, 1183–1196.
57. Göktepe, S.; Acharya, S.N.S.; Wong, J.; Kuhl, E. Computational modeling of passive myocardium. Int. J. Numer. Methods Biomed. Eng. 2011, 27, 1–12.
58. Lee, L.C.; Genet, M.; Acevedo-Bolton, G.; Ordovas, K.; Guccione, J.M.; Kuhl, E. A computational model that predicts reverse growth in response to mechanical unloading. Biomech. Modeling Mechanobiol. 2015, 14, 217–229.
59. Taber, L.A. Theoretical study of Beloussov's hyper-restoration hypothesis for mechanical regulation of morphogenesis. Biomech. Model. Mechanobiol. 2008, 7, 427–441.
60. Hamburger, V.; Hamilton, H.L. A series of normal stages in the development of the chick embryo. Dev. Dyn. 1992, 195, 231–272.
61. Konofagou, E.E.; D'Hooge, J.; Ophir, J. Myocardial elastography—A feasibility study in vivo. Ultrasound Med. Biol. 2002, 28, 475–482.
62. Davey, M.G.; Tickle, C. The chicken as a model for embryonic development. Cytogenet. Genome Res. 2007, 117, 231–239.
63. Sedmera, D.; Pexieder, T.; Rychterova, V.; Hu, N.; Clark, E.B. Remodeling of chick embryonic ventricular myoarchitecture under experimentally changed loading conditions. Anat. Rec. Off. Publ. Am. Assoc. Anat. 1999, 254, 238–252.
64. Al Naieb, S.; Happel, C.M.; Yelbuz, T.M. A detailed atlas of chick heart development in vivo. Ann. Anat. 2013, 195, 324–341.

65. Tobita, K.; Schroder, E.A.; Tinney, J.P.; Garrison, J.B.; Keller, B.B. Regional passive ventricular stress-strain relations during development of altered loads in chick embryo. Am. J. Physiol.-Heart Circ. Physiol. 2002, 282, H2386–H2396.
66. Zamir, E.A.; Taber, L.A. On the effects of residual stress in microindentation tests of soft tissue structures. J. Biomech. Eng. 2004, 126, 276–283.
67. Miller, C.E.; Vanni, M.A.; Taber, L.A.; Keller, B.B. Passive stress–strain measurements in the stage-16 and stage-18 embryonic chick heart. J. Biomech. Eng. 1997, 119, 445–451.
68. Alford, P.W.; Taber, L.A. Regional epicardial strain in the embryonic chick heart during the early looping stages. J. Biomech. 2003, 36, 1135–1141.
69. Taber, L.A.; Chabert, S. Theoretical and experimental study of growth and remodeling in the developing heart. Biomech. Model. Mechanobiol. 2002, 1, 29–43.
70. Zimmerman, F.J.; Hughes, S.F.; Cuneo, B.; Benson, D.W. The effect of cardiac cycle length on ventricular end-diastolic pressure and maximum time derivative of pressure in the stage 24 chick embryo. Pediatr. Res. 1991, 29, 338–346.
71. Zamir, E.A.; Srinivasan, V.; Perucchio, R.; Taber, L.A. Mechanical asymmetry in the embryonic chick heart during looping. Ann. Biomed. Eng. 2003, 31, 1327–1336.
72. Butcher, J.T.; McQuinn, T.C.; Sedmera, D.; Turner, D.; Markwald, R.R. Transitions in early embryonic atrioventricular valvular function correspond with changes in cushion biomechanics that are predictable by tissue composition. Circ. Res. 2007, 100, 1503–1511.
73. Wang, Y.; Dur, O.; Patrick, M.J.; Tinney, J.P.; Tobita, K.; Keller, B.B.; Pekkan, K. Aortic arch morphogenesis and flow modeling in the chick embryo. Ann. Biomed. Eng. 2009, 37, 1069–1081.
74. Celik, M.; Goktas, S.; Karakaya, C.; Cakiroglu, A.I.; Karahuseyinoglu, S.; Lashkarinia, S.S.; Ermek, E.; Pekkan, K. Microstructure of early embryonic aortic arch and its reversibility following mechanically altered hemodynamic load release. Am. J. Physiol Heart Circ. Physiol. 2020, 318, H1208–H1218.
75. Lindsey, S.E.; Menon, P.G.; Kowalski, W.J.; Shekhar, A.; Yalcin, H.C.; Nishimura, N.; Schaffer, C.B.; Butcher, J.T.; Pekkan, K. Growth and

hemodynamics after early embryonic aortic arch occlusion. Biomech. Model. Mechanobiol. 2015, 14, 735–751.

76. Yap, C.H.; Liu, X.; Pekkan, K. Characterization of the vessel geometry, flow mechanics and wall shear stress in the great arteries of wildtype prenatal mouse. PLoS ONE 2014, 9, e86878.
77. Eghtesady, P.; Michelfelder, E.; Altaye, M.; Ballard, E.; Hirsh, R.; Beekman, R.H. 3rd. Revisiting animal models of aortic stenosis in the early gestation fetus. Ann. Thorac. Surg. 2007, 83, 631–639.
78. O'Tierney, P.F.; Anderson, D.F.; Faber, J.J.; Louey, S.; Thornburg, K.L.; Giraud, G.D. Reduced systolic pressure load decreases cell-cycle activity in the fetal sheep heart. Am. J. Physiol. Regul. Integr. Comp. Physiol. 2010, 299, R573-R578.
79. Sacks, M.S.; Yoganathan, A.P. Heart valve function: A biomechanical perspective. Philos Trans. R. Soc. Lond. B Biol. Sci. 2007, 362, 1369–1391.
80. Jett, S.; Laurence, D.; Kunkel, R.; Babu, A.R.; Kramer, K.; Baumwart, R.; Towner, R.; Wu, Y.; Lee, C.H. An investigation of the anisotropic mechanical properties and anatomical structure of porcine atrioventricular heart valves. J. Mech. Behav. Biomed. Mater. 2018, 87, 155–171.
81. Khoiy, K.A.; Pant, A.D.; Amini, R. Quantification of Material Constants for a Phenomenological Constitutive Model of Porcine Tricuspid Valve Leaflets for Simulation Applications. J. Biomech. Eng. 2018, 140.
82. Lodder, J.; Verkerke, G.J.; Delemarre, B.J.; Dodou, D. Morphological and mechanical properties of the posterior leaflet chordae tendineae in the mitral valve. Proc. Inst. Mech. Eng. H 2016, 230, 77–84.
83. Allison, B.J.; Brain, K.L.; Niu, Y.; Kane, A.D.; Herrera, E.A.; Thakor, A.S.; Botting, K.J.; Cross, C.M.; Itani, N.; Skeffington, K.L.; et al. Fetal in vivo continuous cardiovascular function during chronic hypoxia. J. Physiol. 2016, 594, 1247–1264.
84. Segar, J.L.; Hajduczok, G.; Smith, B.A.; Merrill, D.C.; Robillard, J.E. Ontogeny of baroreflex control of renal sympathetic nerve activity and heart rate. Am. J. Physiol. 1992, 263, H1819–H1826.
85. Huhta, H.; Junno, J.; Haapsamo, M.; Erkinaro, T.; Ohtonen, P.; Davis, L.E.; Hohimer, A.R.; Acharya, G.; Rasanen, J. Fetal sheep central haemodynamics

and cardiac function during occlusion of the ascending aorta. Exp. Physiol. 2018, 103, 58–67.

86. Tibayan, F.A.; Louey, S.; Jonker, S.; Espinoza, H.; Chattergoon, N.; You, F.; Thornburg, K.L.; Giraud, G. Increased systolic load causes adverse remodeling of fetal aortic and mitral valves. Am. J. Physiol. Regul. Integr. Comp. Physiol. 2015, 309, R1490–R1498.
87. Rankin, J.H.; Landauer, M.; Tian, Q.; Phernetton, T.M. Cardiovascular responses to forskolin in the ovine fetus. J. Dev. Physiol. 1989, 11, 7–10.
88. Ishiwata, T.; Nakazawa, M.; Pu, W.T.; Tevosian, S.G.; Izumo, S. Developmental changes in ventricular diastolic function correlate with changes in ventricular myoarchitecture in normal mouse embryos. Circ. Res. 2003, 93, 857–865.
89. Sharifi, A.; Gendernalik, A.; Garrity, D.; Bark, D. Valveless pumping behavior of the simulated embryonic heart tube as a function of contractile patterns and myocardial stiffness. Biomech. Model. Mechanobiol. 2021, 20, 2001–2012.
90. Chelliah, A.; Dham, N.; Frank, L.H.; Donofrio, M.; Krishnan, A. Myocardial strain can be measured from first trimester fetal echocardiography using velocity vector imaging. Prenat Diagn. 2016, 36, 483–488.
91. van Geemen, D.; Soares, A.L.; Oomen, P.J.; Driessen-Mol, A.; Janssen-van den Broek, M.W.; van den Bogaerdt, A.J.; Bogers, A.J.; Goumans, M.J.; Baaijens, F.P.; Bouten, C.V. Age-Dependent Changes in Geometry, Tissue Composition and Mechanical Properties of Fetal to Adult Cryopreserved Human Heart Valves. PLoS ONE 2016, 11, e0149020.
92. Emery, J.L.; Omens, J.H.; McCulloch, A.D. Strain softening in rat left ventricular myocardium. J. Biomech. Eng. 1997, 119, 6–12.
93. Espe, E.K.; Aronsen, J.M.; Nordén, E.S.; Zhang, L.; Sjaastad, I. Regional right ventricular function in rats: A novel magnetic resonance imaging method for measurement of right ventricular strain. Am. J. Physiol.-Heart Circ. Physiol. 2020,318, H143–H153.
94. Bolte, C.; Whitsett, J.A.; Kalin, T.V.; Kalinichenko, V.V. Transcription Factors Regulating Embryonic Development of Pulmonary Vasculature. Adv. Anat Embryol Cell Biol. 2018, 228, 1–20.

95. Deng, Y.; Ou, Z.; Li, R.; Chen, Z.; Liang, P.; Sun, L. Affected-embryo-based SNP haplotyping with NGS for the preimplantation genetic testing of Marfan syndrome. Syst Biol. Reprod. Med. 2021, 67, 298–306.
96. Cardoso, S.; Robertson, S.P.; Daniel, P.B. TGFBR1 mutations associated with Loeys-Dietz syndrome are inactivating. J. Recept. Signal. Transduct. Res. 2012, 32, 150–155.
97. Park, A.C.; Phillips, C.L.; Pfeiffer, F.M.; Roenneburg, D.A.; Kernien, J.F.; Adams, S.M.; Davidson, J.M.; Birk, D.E.; Greenspan, D.S. Homozygosity and Heterozygosity for Null Col5a2 Alleles Produce Embryonic Lethality and a Novel Classic Ehlers-Danlos Syndrome-Related Phenotype. Am. J. Pathol. 2015, 185, 2000–2011.
98. Palit, A.; Bhudia, S.K.; Arvanitis, T.N.; Turley, G.A.; Williams, M.A. Computational modelling of left-ventricular diastolic mechanics: Effect of fibre orientation and right-ventricle topology. J. Biomech. 2015, 48, 604–612.
99. Kathiriya, I.S.; Srivastava, D. Left-right asymmetry and cardiac looping: Implications for cardiac development and congenital heart disease. Am. J. Med. Genet. 2000, 97, 271–279.
100. Huang, Y.; Zheng, L.; Gong, X.; Jia, X.; Song, W.; Liu, M.; Fan, Y. Effect of cyclic strain on cardiomyogenic differentiation of rat bone marrow derived mesenchymal stem cells. PLoS ONE 2012, 7, e34960.
101. Cattaruzza, M.; Guzik, T.J.; Slodowski, W.; Pelvan, A.; Becker, J.; Halle, M.; Buchwald, A.B.; Channon, K.M.; Hecker, M. Shear stress insensitivity of endothelial nitric oxide synthase expression as a genetic risk factor for coronary heart disease. Circ. Res. 2004, 95, 841–847.
102. Groenendijk, B.C.; Van der Heiden, K.; Hierck, B.P.; Poelmann, R.E. The role of shear stress on ET-1, KLF2, and NOS-3 expression in the developing cardiovascular system of chicken embryos in a venous ligation model. Physiology 2007, 22, 380–389.
103. Egorova, A.D.; Van der Heiden, K.; Van de Pas, S.; Vennemann, P.; Poelma, C.; DeRuiter, M.C.; Goumans, M.J.; Gittenberger-de Groot, A.C.; ten Dijke, P.; Poelmann, R.E.; et al. Tgfbeta/Alk5 signaling is required for shear stress induced klf2 expression in embryonic endothelial cells. Dev. Dyn. 2011, 240, 1670–1680.

104. Kumar, S.D.; Yong, S.K.; Dheen, S.T.; Bay, B.H.; Tay, S.S. Cardiac malformations are associated with altered expression of vascular endothelial growth factor and endothelial nitric oxide synthase genes in embryos of diabetic mice. Exp. Biol. Med. 2008, 233, 1421–1432.
105. Lacolley, P.; Challande, P.; Osborne-Pellegrin, M.; Regnault, V. Genetics and pathophysiology of arterial stiffness. Cardiovasc. Res. 2009, 81, 637–648.
106. Li, Y.; Zheng, J.; Bird, I.M.; Magness, R.R. Effects of pulsatile shear stress on nitric oxide production and endothelial cell nitric oxide synthase expression by ovine fetoplacental artery endothelial cells. Biol. Reprod. 2003, 69, 1053–1059.
107. Novodvorsky, P.; Chico, T.J. The role of the transcription factor KLF2 in vascular development and disease. Prog. Mol. Biol. Transl. Sci. 2014, 124, 155–188.
108. Malek, A.M.; Zhang, J.; Jiang, J.; Alper, S.L.; Izumo, S. Endothelin-1 gene suppression by shear stress: Pharmacological evaluation of the role of tyrosine kinase, intracellular calcium, cytoskeleton, and mechanosensitive channels. J. Mol. Cell Cardiol. 1999, 31, 387–399.
109. Halabi, C.M.; Broekelmann, T.J.; Lin, M.; Lee, V.S.; Chu, M.L.; Mecham, R.P. Fibulin-4 is essential for maintaining arterial wall integrity in conduit but not muscular arteries. Sci. Adv. 2017, 3, e1602532.
110. Staiculescu, M.C.; Cocciolone, A.J.; Procknow, J.D.; Kim, J.; Wagenseil, J.E. Comparative gene array analyses of severe elastic fiber defects in late embryonic and newborn mouse aorta. Physiol. Genom. 2018, 50, 988–1001.
111. Igoucheva, O.; Alexeev, V.; Halabi, C.M.; Adams, S.M.; Stoilov, I.; Sasaki, T.; Arita, M.; Donahue, A.; Mecham, R.P.; Birk, D.E.; et al. Fibulin-4 E57K Knock-in Mice Recapitulate Cutaneous, Vascular and Skeletal Defects of Recessive Cutis Laxa 1B with both Elastic Fiber and Collagen Fibril Abnormalities. J. Biol. Chem. 2015, 290, 21443–21459.
112. Kim, J.; Procknow, J.D.; Yanagisawa, H.; Wagenseil, J.E. Differences in genetic signaling, and not mechanical properties of the wall, are linked to ascending aortic aneurysms in fibulin-4 knockout mice. Am. J. Physiol. Heart Circ. Physiol. 2015, 309, H103–H113.

113. Stephens, E.H.; Post, A.D.; Laucirica, D.R.; Grande-Allen, K.J. Perinatal changes in mitral and aortic valve structure and composition. Pediatr Dev. Pathol. 2010, 13, 447–458.
114. Toda, M.; Yamamoto, K.; Shimizu, N.; Obi, S.; Kumagaya, S.; Igarashi, T.; Kamiya, A.; Ando, J. Differential gene responses in endothelial cells exposed to a combination of shear stress and cyclic stretch. J. Biotechnol. 2008, 133, 239–244.
115. Montgomery, M.O.; Jiao, Y.; Phillips, S.J.; Singh, G.; Xu, J.; Balsara, R.; Litvin, J. Alterations in sheep fetal right ventricular tissue with induced hemodynamic pressure overload. Basic Res. Cardiol. 1998, 93, 192–200.
116. Zhao, Z. Cardiac malformations and alteration of TGFbeta signaling system in diabetic embryopathy. Birth Defects Res. B Dev. Reprod. Toxicol. 2010, 89, 97–105.
117. Marjolijn Renard, Tammy Holm, Regan Veith, Bert L Callewaert, Lesley C Adès, Osman Baspinar, Angela Pickart, Majed Dasouki, Juliane Hoyer, Anita Rauch, et al. Altered TGFbeta signaling and cardiovascular manifestations in patients with autosomal recessive cutis laxa type I caused by fibulin-4 deficiency. Eur J Hum Genet. 2010, 18, 895¬–901.
118. Ai, J.; Zhang, R.; Gao, X.; Niu, H.F.; Wang, N.; Xu, Y.; Li, Y.; Ma, N.; Sun, L.H.; Pan, Z.W.; et al. Overexpression of microRNA-1 impairs cardiac contractile function by damaging sarcomere assembly. Cardiovasc. Res. 2012, 95, 385–393.
119. Witman, N.; Heigwer, J.; Thaler, B.; Lui, W.O.; Morrison, J.I. miR-128 regulates non-myocyte hyperplasia, deposition of extracellular matrix and Islet1 expression during newt cardiac regeneration. Dev. Biol. 2013, 383, 253–263.
120. Bowen, C.J.; Zhou, J.; Sung, D.C.; Butcher, J.T. Cadherin-11 coordinates cellular migration and extracellular matrix remodeling during aortic valve maturation. Dev. Biol. 2015, 407, 145–157.
121. Sung, D.C.; Bowen, C.J.; Vaidya, K.A.; Zhou, J.; Chapurin, N.; Recknagel, A.; Zhou, B.; Chen, J.; Kotlikoff, M.; Butcher, J.T. Cadherin-11 Overexpression Induces Extracellular Matrix Remodeling and Calcification in

Mature Aortic Valves. Arterioscler. Thromb. Vasc. Biol. 2016, 36, 1627–1637.

122. Lehoux S, Tedgui A. Cellular mechanics and gene expression in blood vessels. J Biomech. 2003, 36, 631–643.
123. Lehoux, S.; Castier, Y.; Tedgui, A. Molecular mechanisms of the vascular responses to haemodynamic forces. J. Intern. Med. 2006, 259, 381–392.
124. Luyckx I, MacCarrick G, Kempers M, Meester J, Geryl C, Rombouts O, et al. Confirmation of the role of pathogenic SMAD6 variants in bicuspid aortic valve-related aortopathy. Eur J Hum Genet. 2019, 27, 1044–1053.
125. Tseng, C.C.S.; Huibers, M.M.H.; van Kuik, J.; de Weger, R.A.; Vink, A.; de Jonge, N. The Interleukin-33/ST2 Pathway Is Expressed in the Failing Human Heart and Associated with Pro-fibrotic Remodeling of the Myocardium. J. Cardiovasc. Transl. Res. 2018, 11, 15–21.
126. Veeraveedu, P.T.; Sanada, S.; Okuda, K.; Fu, H.Y.; Matsuzaki, T.; Araki, R.; Yamato, M.; Yasuda, K.; Sakata, Y.; Yoshimoto, T.; et al. Ablation of IL-33 gene exacerbate myocardial remodeling in mice with heart failure induced by mechanical stress. Biochem. Pharmacol. 2017, 138, 73–80.
127. O'Shaughnessy, K.M. Genetics of arterial structure and function: towards new biomarkers for aortic stiffness? Clin. Sci. 2008, 114, 661–677.
128. Carta, L.; Wagenseil, J.E.; Knutsen, R.H.; Mariko, B.; Faury, G.; Davis, E.C.; Starcher, B.; Mecham, R.P.; Ramirez, F. Discrete contributions of elastic fiber components to arterial development and mechanical compliance. Arterioscler. Thromb. Vasc. Biol. 2009, 29, 2083–2089.
129. Wagenseil, J.E.; Mecham, R.P. Elastin in large artery stiffness and hypertension. J. Cardiovasc. Transl. Res. 2012, 5, 264–273.
130. Bordeleau, F.; Mason, B.N.; Lollis, E.M.; Mazzola, M.; Zanotelli, M.R.; Somasegar, S.; Califano, J.P.; Montague, C.; LaValley, D.J.; Huynh, J.; et al. Matrix stiffening promotes a tumor vasculature phenotype. Proc. Natl. Acad. Sci. USA 2017, 114, 492–497.
131. Makwana, O.; King, N.M.; Ahles, L.; Selmin, O.; Granzier, H.L.; Runyan, R.B. Exposure to low-dose trichloroethylene alters shear stress gene expression and function in the developing chick heart. Cardiovasc. Toxicol. 2010, 10, 100–107.

132. Gould, R.A.; Aziz, H.; Woods, C.E.; Seman-Senderos, M.A.; Sparks, E.; Preuss, C.; Wünnemann, F.; Bedja, D.; Moats, C.R.; McClymont, S.A.; et al. ROBO4 variants predispose individuals to bicuspid aortic valve and thoracic aortic aneurysm. Nat. Genet. 2019, 51, 42–50.
133. Koenig, S.N.; LaHaye, S.; Feller, J.D.; Rowland, P.; Hor, K.N.; Trask, A.J.; Janssen, P.M.; Radtke, F.; Lilly, B.; Garg, V. Notch1 haploinsufficiency causes ascending aortic aneurysms in mice. JCI Insight 2017, 2, e91353.
134. Laurent, S.; Boutouyrie, P.; Lacolley, P. Structural and genetic bases of arterial stiffness. Hypertension 2005, 45, 1050–1055.
135. Puzzi, L.; Borin, D.; Gurha, P.; Lombardi, R.; Martinelli, V.; Weiss, M.; Andolfi, L.; Lazzarino, M.; Mestroni, L.; Marian, A.J.; et al. Knock Down of Plakophillin 2 Dysregulates Adhesion Pathway through Upregulation of miR200b and Alters the Mechanical Properties in Cardiac Cells. Cells 2019, 8, 1639.

CHAPTER 2 REFERENCES

1. Karakaya, C., et al., Asymmetry in Mechanosensitive Gene Expression during Aortic Arch Morphogenesis. Sci Rep, 2018. 8(1): p. 16948.
2. Muramatsu, T., et al., Comparison of three nonviral transfection methods for foreign gene expression in early chicken embryos in Ovo. Biochem Biophys Res Commun, 1997. 230(2): p. 376-80.
3. Krull, C.E., A primer on using in Ovo electroporation to analyze gene function. Dev Dyn, 2004. 229(3): p. 433-9.
4. Voiculescu, O., C. Papanayotou, and C.D. Stern, Spatially and temporally controlled electroporation of early chick embryos. Nat Protoc, 2008. 3(3): p. 419-26.
5. Nakamura, H., Y. Watanabe, and J. Funahashi, Misexpression of genes in brain vesicles by in Ovo electroporation. Dev Growth Differ, 2000. 42(3): p. 199-201.
6. Nakamura, H. and J. Funahashi, Introduction of DNA into chick embryos by in Ovo electroporation. Methods, 2001. 24(1): p. 43-8.
7. Momose, T., et al., Efficient targeting of gene expression in chick embryos by microelectroporation. Dev Growth Differ, 1999. 41(3): p. 335-44.

8. Katahira, T. and H. Nakamura, Gene silencing in chick embryos with a vector-based small interfering RNA system. Dev Growth Differ, 2003. 45(4): p. 361-7.
9. Chen, Y.X. and C.E. Krull, Using in Ovo electroporation to transfect cells in avian somites. CSH Protoc, 2008. 2008: p. pdb prot4924.
10. Pekarik, V., et al., Screening for gene function in chicken embryo using RNAi and electroporation. Nat Biotechnol, 2003. 21(1): p. 93-6.
11. Voiculescu, O. and C.D. Stern, Manipulating Gene Expression in the Chick Embryo. Methods Mol Biol, 2017. 1565: p. 105-114.
12. Nakamura, H., et al., Gain- and loss-of-function in chick embryos by electroporation. Mech Dev, 2004. 121(9): p. 1137-43.
13. Ueda, S., T. Suzuki, and M. Tanaka, Transgene Introduction into the Chick Limb Bud by Electroporation. Methods Mol Biol, 2017. 1650: p. 203-208.
14. McLennan, R. and P.M. Kulesa, In Ovo Electroporation of Plasmid DNA and Morpholinos into Specific Tissues During Early Embryogenesis. Methods Mol Biol, 2019. 1976: p. 71-82.
15. Stark, D.A. and P.M. Kulesa, Photoactivatable green fluorescent protein as a single-cell marker in living embryos. Dev Dyn, 2005. 233(3): p. 983-92.
16. Norris, A. and A. Streit, Morpholinos: studying gene function in the chick. Methods, 2014. 66(3): p. 454-65.
17. Broderick, K.E., et al., Optimized in vivo transfer of small interfering RNA targeting dermal tissue using in vivo surface electroporation. Mol Ther Nucleic Acids, 2012. 1: p. e11.
18. Itasaki, N., S. Bel-Vialar, and R. Krumlauf, 'Shocking' developments in chick embryology: electroporation and in Ovo gene expression. Nat Cell Biol, 1999. 1(8): p. E203-7.
19. Peng, H., Y. Wu, and Y. Zhang, Efficient delivery of DNA and morpholinos into mouse preimplantation embryos by electroporation. PLoS One, 2012. 7(8): p. e43748.
20. Chen, Y., et al., Characterization of chicken Nf2/merlin indicates regulatory roles in cell proliferation and migration. Dev Dyn, 2004. 229(3): p. 541-54.

21. Baeriswyl, T. and E.T. Stoeckli, In Ovo RNAi opens new possibilities for temporal and spatial control of gene silencing during development of the vertebrate nervous system. J RNAi Gene Silencing, 2006. 2(1): p. 126-35.
22. Hamburger, V., The stage series of the chick embryo. Dev Dyn, 1992. 195(4): p. 273-5.
23. Livak, K.J. and T.D. Schmittgen, Analysis of relative gene expression data using real-time quantitative PCR and the 2(-Delta Delta C(T)) Method. Methods, 2001. 25(4): p. 402-8.
24. Wang, Y., et al., Aortic arch morphogenesis and flow modeling in the chick embryo. Ann Biomed Eng, 2009. 37(6): p. 1069-81.
25. Panina, Y., et al., Validation of Common Housekeeping Genes as Reference for qPCR Gene Expression Analysis During iPS Reprogramming Process. Sci Rep, 2018. 8(1): p. 8716.
26. Cai, D.H., et al., MMP-2 expression during early avian cardiac and neural crest morphogenesis. Anat Rec, 2000. 259(2): p. 168-79.
27. Li, T., et al., TLR4 and MMP2 polymorphisms and their associations with cardiovascular risk factors in susceptibility to aortic aneurysmal diseases. Biosci Rep, 2019. 39(1).
28. Barhoumi, T., et al., Matrix metalloproteinase-2 knockout prevents angiotensin II-induced vascular injury. Cardiovasc Res, 2017. 113(14): p. 1753-1762.
29. Chakrabarti, M., et al., Transforming Growth Factor Beta3 is Required for Cardiovascular Development. J Cardiovasc Dev Dis, 2020. 7(2).
30. Dabek, J., et al., Transforming growth factor beta and cardiovascular diseases: the other facet of the 'protective cytokine'. Pharmacol Rep, 2006. 58(6): p. 799-805.
31. Goumans, M.J. and P. Ten Dijke, TGF-beta Signaling in Control of Cardiovascular Function. Cold Spring Harb Perspect Biol, 2018. 10(2).
32. Bravo-Jaimes, K. and S.K. Prakash, Genetics in bicuspid aortic valve disease: Where are we? Prog Cardiovasc Dis, 2020. 63(4): p. 398-406.
33. Low, E.L., A.H. Baker, and A.C. Bradshaw, TGFbeta, smooth muscle cells and coronary artery disease: a review. Cell Signal, 2019. 53: p. 90-101.

34. Bertoli-Avella, A.M., et al., Mutations in a TGF-beta ligand, TGFB3, cause syndromic aortic aneurysms and dissections. J Am Coll Cardiol, 2015. 65(13): p. 1324-1336.
35. Doetschman, T., et al., Transforming growth factor beta signaling in adult cardiovascular diseases and repair. Cell Tissue Res, 2012. 347(1): p. 203-23.